Real-Time Simulation of Service Vessels for Offshore Wind Turbine

Master Thesis

rampionoffshore.com

Real-Time Simulation of Service Vessels for Offshore Wind Turbine

Master Thesis
February 11, 2024

By
Jose Maria San Nicolas Mendez

Approval

This thesis has been prepared over six months at the Department of Civil Mechanical Engineering, at the Technical University of Denmark, DTU, in partial fulfilment for the degree Master of Science in Engineering, MSc Eng.

It is assumed that the reader has a basic knowledge in the areas of marine and ocean engineering.

Jose Maria San Nicolas Mendez - s222745

Abstract

The present project focuses on how the scattered wave field generated by the presence of fixed offshore structures, i.e. bottom-mounted wind turbines, influences the ship's response amplitude. It is worth mentioning that only the F-K forcing of the scattered wave from the cylinder is considered, i.e. the project disregards a potential scattered wave field generated by the ship's interaction with the scattered wave from the cylinder. Therefore, the ship is not generating any scattered wave field; only the cylinder.

By using WAMIT and MATLAB, the response Amplitude Operator (RAO) of both situations, i.e. "Open sea" and "With cylinder", are compared in a regular sea state for different heading angles β. These comparisons have indicated that there are indeed reasons to believe the heading angle plays an important role in safety matters when performing any kind of wind farm operation.

Finally, an extension of the MATLAB code is adapted to the FORCETechnology procedure when evaluating a real-time domain ship's response to incoming irregular waves.

Acknowledgements

Contents

1 Introduction

Addressing safety and operability challenges for ships in adverse sea conditions is complex, especially during open-sea operations. Numerous experiments at the model scale and full scale accurately study ship motions although it may be costly compared to a computational analysis.

This project's scope is to perform accurate real-time simulations of ocean waves around off-shore wind turbine foundations and real-time calculations of ocean wave forces on service vessels. The study starts with a comprehensive analysis of all six degrees of freedom under a constant sea state (regular waves) and extends to irregular waves while accounting for the influence of the scattered wave field caused by the presence of the wind turbine foundation.

Two different ship designs have been used to perform the analysis of motions under both regular and irregular waves: Wigley Hull and a typical workboat designed and provided by Steffan Brandt Tolboe. The former is a parameterised boat which can be easily modelled and frequently used to perform tests while the latter has been rigorously designed to perform efficiently wind farm operations.

The scattered wave field is first analytically worked out with the exact solution of the diffraction effects around a cylinder [1], then implemented and validated in Matlab through the BEM ensuring convergence is achieved. Once it is accomplished, the scattered force can be included as a prescribed external force along with the F-K force, computed with WAMIT, and finally obtain the RAOs, where the influence of the cylinder can be observed.

It is also paramount not to forget about the wave heading angle during this operation. Motions like Roll, which is crucial for ship operability [2], are response-sensitive to sea waves; others, like Heave, are not. Depending on the situation, these issues can be addressed with a certain simplicity by modifying the heading angle.

2 Background and Case Study Parameters

2.1 Location

Horns Rev III, approximately $30\,\mathrm{km}$ off the Danish Jutland coast (North Sea), will be a reference in this study, by importing the dimensions of the wind turbine foundations (i.e. monopile of $6.5\,\mathrm{m}$ diameter) and the wave climate in that location.

2.2 Climate study

This section is focused on the establishment of a most probable range of the non-dimensional wave number, i.e. ka (where k is the wave number and a is the cylinder radius), that takes place at Horns Rev 3 wind farm. To do so, it is necessary to study thoroughly and separately wind waves and swell.

Both types of waves will induce a different range of ka since they have inverse characteristics. While wind waves have a high frequency and small wavelength, swell waves are known to have a shorter frequency and larger wavelength.

Wavelength and its interaction with the wind turbine foundation are key to studying the diffraction effects (explained in Section 3.1) and thus, the importance of the scattered wave field on the ship.

The following figure depicts a scattered density distribution plot of wind waves in Horns Rev III during 2022 [3]. It can be noted that the range of both Mean period and Significant wave height is quite large but narrow-banded. Leaving out outsider points, a representative wind wave climate would have a mean period from $1.8\,\mathrm{s}$ up to $8\,\mathrm{s}$ with their corresponding ka values: 4 and 0.2, respectively.
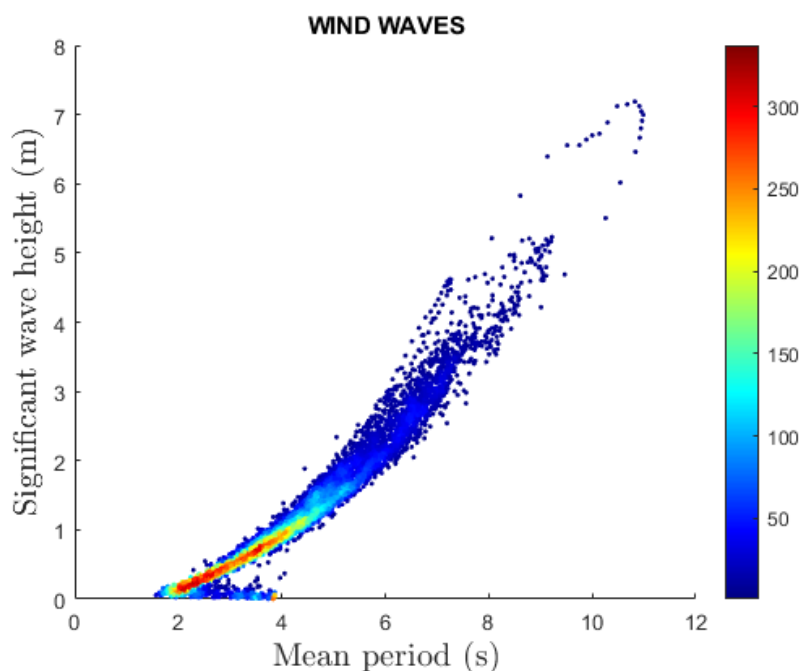

Figure 2.1: Density plot of Wind waves.

Conversely, Swell waves wave climate is rather scattered (see Fig. 2.2) [3]. Note also that swell waves have a lower frequency, giving a most probable non-dimensional wave number range of 0.1 to 1.45 (i.e. $11\,\text{s}$ and $3\,\text{s}$, respectively).

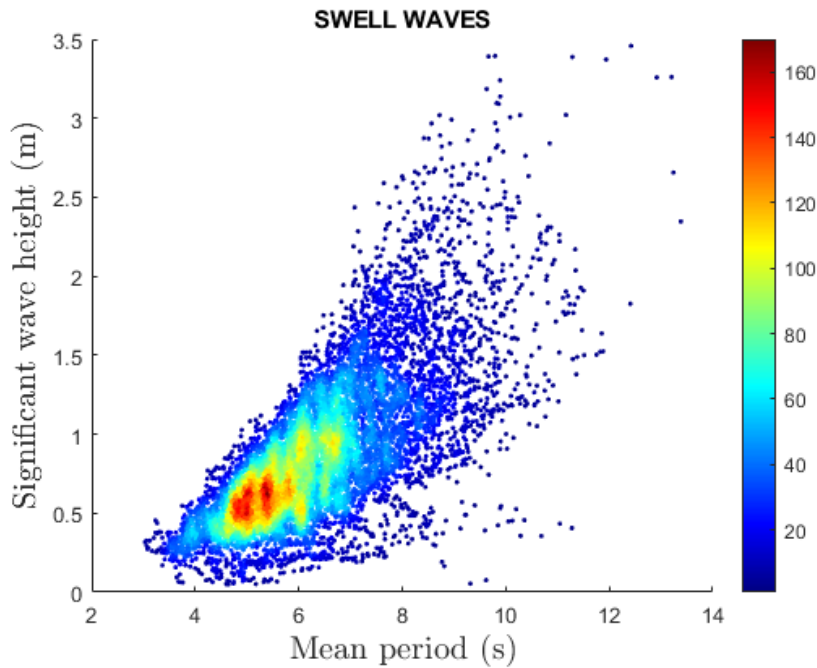
Figure 2.2: Density plot of Swell waves.

Therefore, the most probable range of ka can be set as 0.1 to 4, corresponding to a wavelength of $189\,\text{m}$ and $5\,\text{m}$; respectively.

2.3 Working conditions. Operatibility

2.3.1 Wind farm ships

When it comes to wind farm operations, there is a wide variety of them that can be performed by different kinds of ships e.g., wind farm operations vessels, known as SOVs, CSOVs, installation vessels, or jack-up barges, all of them playing a crucial role in every phase of offshore wind farm operations. Some of the tasks these vessels are important can be crew transportation, construction, maintenance, and the eventual decommissioning of wind turbines, even in some of the most challenging ocean conditions [4].

International standards and regulations encompass a wide array of aspects, starting from the design and construction stages. Wind farm vessels must adhere to specific guidelines and requirements to guarantee their structural integrity and stability and, even under adverse weather conditions, they must provide a secure working environment for the crew involved in wind farm activities.

2.3.2 Wind farm operations

Health, Safety, and Environment (HSE) constitute three of the most key elements across industries, but their value escalates considerably within offshore wind farm operations.

The offshore wind energy sector presents unique challenges that demand meticulous oversight, given the presence of unfavourable weather conditions, complex machinery, and considerable distances from the coastline. Such challenges need to be addressed

with an elevated emphasis on safety and sustainability by the HSE department, responsible for safety procedures and protocols implementation, employee training, ongoing monitoring, and assessment of offshore wind farm activities, execution of emergency response plans, etc [4].

2.3.3 Wave height and accessibility

All the regulations, requirements, guidelines, and safety measures previously mentioned need to be carried out within a secure wave climate environment.

Weather conditions are a paramount element to consider when performing wind farm operations. The ability to reach an offshore wind turbine via ship primarily hinges on wave height. Typically, weather conditions featuring a substantial wave height (Hs) exceeding $1.5\,$m are categorized as "Weather Days." As section 2.3.1 states, there is a wide range of wind farm operations and wind farm ships, each of them with different purposes and safety measures; however, beyond the "Weather days" point, even transferring service personnel from a work vessel to the offshore installation ladder becomes too dangerous. Even with specialized access systems designed to counteract the ship's motion, gaining access to offshore wind turbines is feasible only up to a significant wave height of approximately $2\,$m [5].

Real-Time Simulation of Service Vessels for Offshore Wind Turbine

3 Theory

3.1 Wave diffraction around a cylinder

This section focuses on diffraction effects. These effects become relevant when the ratio D/L is greater than 0.2, where D is the diameter of the wind turbine foundation and L is the incident wavelength [6].

A $6.5\,\text{m}$ cylindrical monopile is analyzed for the case study. That means diffraction effects will occur around the wind turbine foundation whenever the incident wavelength is $33\,\text{m}$ or shorter. On one side of the cylinder (the front part), the incident wave will be reflected in the opposite direction (wave moving outwards) whereas on the sheltered side, the wavefronts are bent around the cylinder.
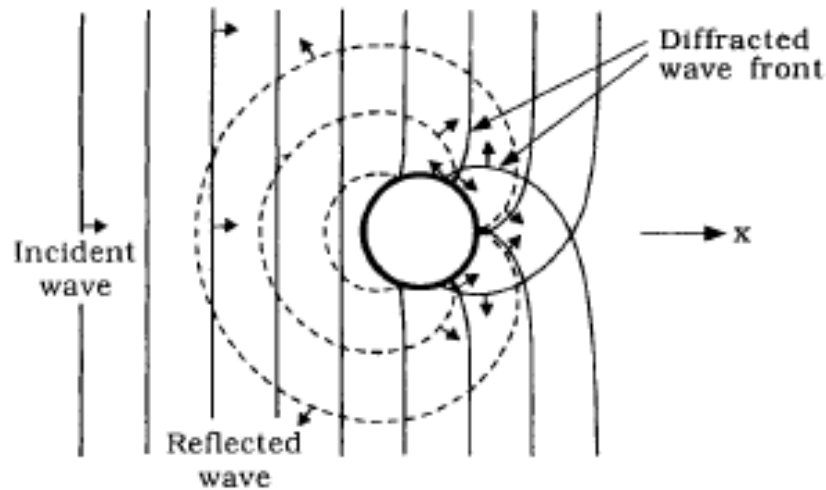

Figure 3.1: Sketch of the incident, diffracted and reflected wave fronts for a vertically placed cylinder [6].

Regarding the flow around the cylinder in the diffraction flow regime, we can assume it is unseparated. In order to prove so, the KC number, Eq. (3.1) and maximum wave steepness ratio, Eq. (3.2) must be considered.

$$KC = \frac{2\pi a}{D} = \frac{\pi\,(H/L)}{(D/L)\,\mathsf{tanh}(kh)} \tag{3.1}$$

where H is the wave height, L; the wavelength, k; the wave number and h; the water depth.

$$\left(\frac{H}{L}\right)_{max} = 0.14\,\mathsf{tanh}(kh) \tag{3.2}$$

Computing Eqs. (3.1) and (3.2) leads to Fig. 3.2 where it can be seen that diffraction takes place for such small values of KC number, namely $KC < 2$. For KC greater than

2, waves will break, hence, there is no flow separation in the diffraction regime. Since the wavelength is considered much larger than the wave height during the working conditions, it can therefore be assumed there is no flow separation, i.e. $KC < 2$.
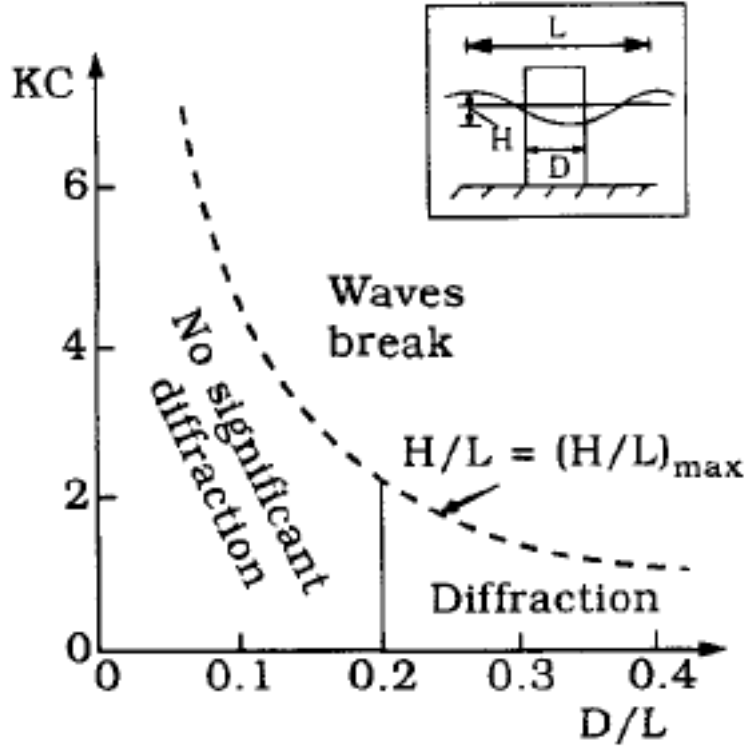

Figure 3.2: Flow regimes in terms of KC and D/L [6].

3.1.1 MacCamy and Fuchs Solution

MacCamy and Fuchs (1954) [1] developed an analytical solution applying potential flow theory, i.e. no flow separation, to describe the diffraction effects for water waves incident on a vertical cylinder of circular cross-section in finite water depth.

In addition, by assuming linear wave theory, i.e. the wave height is much smaller than the wavelength, some approximations can be made such as linear superposition [1]. For a time-harmonic wave at frequency ω, the total velocity potential can be written:

$$\Phi = \Re\left\{\phi(x, y, z, \omega)\, e^{i\omega t}\right\} \tag{3.3}$$

$$\phi = \phi_0 + \phi_s \tag{3.4}$$

where ϕ_0 is the potential function of the undisturbed incident wave approaching the cylinder from $x \sim -\infty$ and ϕ_s is the scattered wave due to the cylinder.

The potential function ϕ fulfils the following linear boundary value problem:

- The continuity equation:

$$\nabla^2\phi = \frac{\partial^2\phi}{\partial x^2} + \frac{\partial^2\phi}{\partial y^2} + \frac{\partial^2\phi}{\partial z^2} = 0 \tag{3.5}$$

Real-Time Simulation of Service Vessels for Offshore Wind Turbine

- No velocity through the bed:

$$\frac{\partial \phi}{\partial z} = 0 \quad \text{at} \quad z = -h \tag{3.6}$$

- The combined free surface boundary condition:

$$\frac{\partial^2 \phi}{\partial t^2} + g \frac{\partial \phi}{\partial z} = 0 \quad \text{at} \quad z = 0 \tag{3.7}$$

- No normal velocity at the body surface:

$$\frac{\partial \phi}{\partial r} = 0 \quad \text{at the body surface} \tag{3.8}$$

From the linear theory, the **incident potential function** ϕ_0 is obtained:

$$\phi_0 = \mathrm{i}\frac{gH}{2\omega} \frac{\cosh(k(z+h))}{\cosh(kh)} \mathrm{e}^{-\mathrm{i}kx} \tag{3.9}$$

where the z-axis points positively upwards from the mean water level. The cylindrical wavefronts are assumed to approach the circular cylinder of radius a from $x \sim -\infty$.

Introducing now polar coordinates to Eq. (3.9) where

$$\begin{aligned} x &= r \cos\theta \\ y &= r \sin\theta \end{aligned} \tag{3.10}$$

the potential function takes the form:

$$\phi_0 (r, \theta, z) = \mathrm{i}\frac{gH}{2\omega} \frac{\cosh(k(z+h))}{\cosh(kh)} \mathrm{e}^{-\mathrm{i}kr\cos\theta} \tag{3.11}$$

and utilizing the linear dynamic free-surface condition, which requires that the pressure on the free surface is equal to the atmospheric pressure, the incident wave elevation can be derived as

$$\eta_0 (r, \theta, t) = -\frac{1}{g}\frac{\partial \phi}{\partial t}(z = 0) = \Re \left\{ A \mathrm{e}^{\mathrm{i}(\omega t - kr\cos\theta)} \right\}, \tag{3.12}$$

where $A = H/2$ is the wave amplitude and the last term can be written in terms of the Bessel functions J_m, starting from $m = 0$ up to a certain value that ensures the accuracy required:

$$e^{-\mathrm{i}kr\cos\theta} = \sum_{m=0}^{\infty} \varepsilon_m (-\mathrm{i})^m J_m(kr) \cos(m\theta) \tag{3.13}$$

with $\epsilon_0 = 1$ and $\epsilon_m = 2$ for $m \geq 1$.

Concerning the second part of Eq. (3.3), the **scattered potential function** [7] ϕ_s is presumed to have a similar form to Eq. (3.11) and symmetric shape for θ, i.e., $\phi_s(-\theta) = \phi_s(\theta)$ while satisfying the no-flux condition of the total potential on the cylinder boundary, that is

$$\frac{\partial \phi_s}{\partial n} = -\frac{\partial \phi_0}{\partial n} \rightarrow \frac{\partial \phi_s}{\partial r} = -\frac{\partial \phi_0}{\partial r} \quad \text{on } r = a. \tag{3.14}$$

The far-field condition that ensures that waves propagate outwards from the cylinder and vanish as $r \rightarrow \infty$, with an asymptotic form, is satisfied by using a linear combination of the Bessel Functions, in this case, the Hankel Function. Therefore, the scattered potential function and its corresponding free surface elevation can be written, respectively, as

$$\phi_s(r, \theta, z) = \frac{\mathrm{i}g}{\omega} \frac{\cosh(k(z+h))}{\cosh(kh)} \eta_s(r, \theta), \tag{3.15}$$

$$\eta_s(r, \theta) = \sum_{m=0}^{\infty} H_m^{(2)}(kr)(\alpha_{0m} \cos m\theta + \beta_{0m} \sin m\theta). \tag{3.16}$$

where $H_m^{(2)}(kr)$ is Hankel function of the second kind:

$$H_m^{(2)}(kr) = J_m(kr) - \mathrm{i}Y_m(kr) \rightarrow \sqrt{\frac{2}{\pi kr}} e^{-\mathrm{i}\left(kr - \frac{m\pi}{2} - \frac{\pi}{4}\right)} \quad \text{as } r \rightarrow \infty. \tag{3.17}$$

Here, Y_m is the Bessel function of the second kind. Coefficients α_{0m} and β_{0m} can be derived by invoking the boundary condition, using Eq. (3.13), resulting in

$$\alpha_{0m} = -\varepsilon_m(-\mathrm{i})^m \frac{J_m'(ka)}{H_m^{(1)'}(ka)} \tag{3.18}$$

$$\beta_{0m} = 0,$$

Lastly, to obtain the **total potential function**, only one step is left: summing ϕ_0 and ϕ_s from Eqs. (3.11) and (3.15), respectively. The solution is then:

$$\phi(r, \theta, z) = \mathrm{i}\frac{gA}{\omega} \frac{\cosh[k(z+h)]}{\cosh(kh)}$$
$$\sum_{m=0}^{\infty} \varepsilon_m(-\mathrm{i})^m \left[J_m(kr) - \frac{J_m'(ka)}{H_m^{(2)'}(ka)} H_m^{(2)}(kr) \right] \cos(m\theta), \tag{3.19}$$

where the prime denotes the derivative with respect to the argument. The dynamic pressure is given by

$$p(r, \theta, z) = \mathrm{i}\omega\rho\phi = \rho g \eta \frac{\cosh[k(z+h)]}{\cosh kh}. \tag{3.20}$$

Adapting this equation to a cylinder of radius a, the non-dimensional pressure at any point on the cylinder surface due to the scattered wave may be calculated as

$$\frac{p}{\rho g A} = \frac{\cosh\left[k(z+h)\right]}{\cosh\left(kh\right)} \sum_{m=0}^{\infty} -\varepsilon_m(-\mathrm{i})^m \frac{J_m'\left(ka\right)}{H_m^{(2)\prime}\left(ka\right)} H_m^{(2)}(kr) \cos(m\theta), \tag{3.21}$$

and the corresponding force on a nearby structure is

$$F_j^s = \int_{S_b} p\, n_j\, dS, \tag{3.22}$$

where S_b corresponds to the submerged body surface and n_j to the generalized unit normal vector in direction j.

3.2   Validation of the analytical solution

This section aims to validate the analytical solution from MacCamy and Fuchs and implement a scattered wave elevation code in Matlab that works for a sufficiently large region around a cylinder for all possible angles. Apart from Eqs. (3.16) and (3.18), thanks to linear superposition, the non-dimensional scattered wave elevation can also be obtained from Eq. (3.19) by subtracting the summation term relative to the Bessel function expansion of the exponential (Eq. (3.13)), resulting in

$$\eta_s(r,\theta) = \sum_0^M -\varepsilon_m\left(-i\right)^m \left[\frac{J_m'\left(ka\right)}{H_m^{(2)\prime}\left(ka\right)} H_m^{(2)}(kr)\right] \cos(m\theta), \tag{3.23}$$

In this case, $m = 0, 1, ..., M$, where M corresponds to a sufficiently large number of iterations to achieve the accuracy threshold of 10e-6 in results.

Fig. 3.3 depicts an example of the scattered wave elevation around a cylinder of $6.5\,\mathrm{m}$ diameter due to a $ka = 4$.
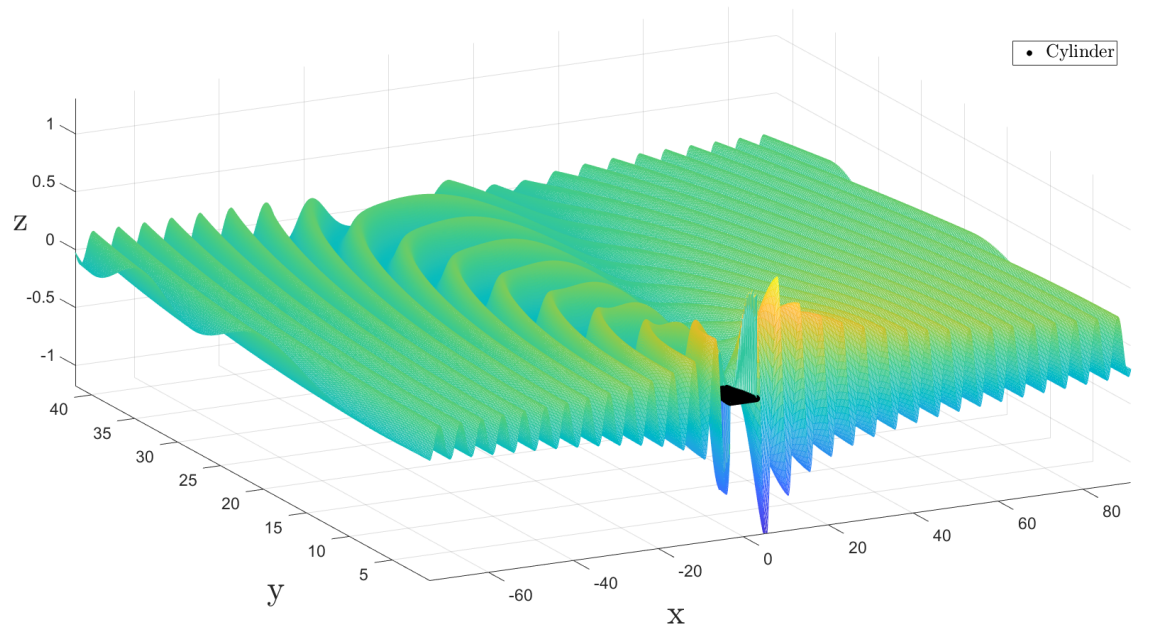

Figure 3.3: Scattered wave elevation

As a way to validate the equation implemented in Matlab, inspiration from [1] has been drawn by plotting the polar distribution of run-up around a circular cylinder for different non-dimensional wavelengths, ka, see Fig. 3.4.
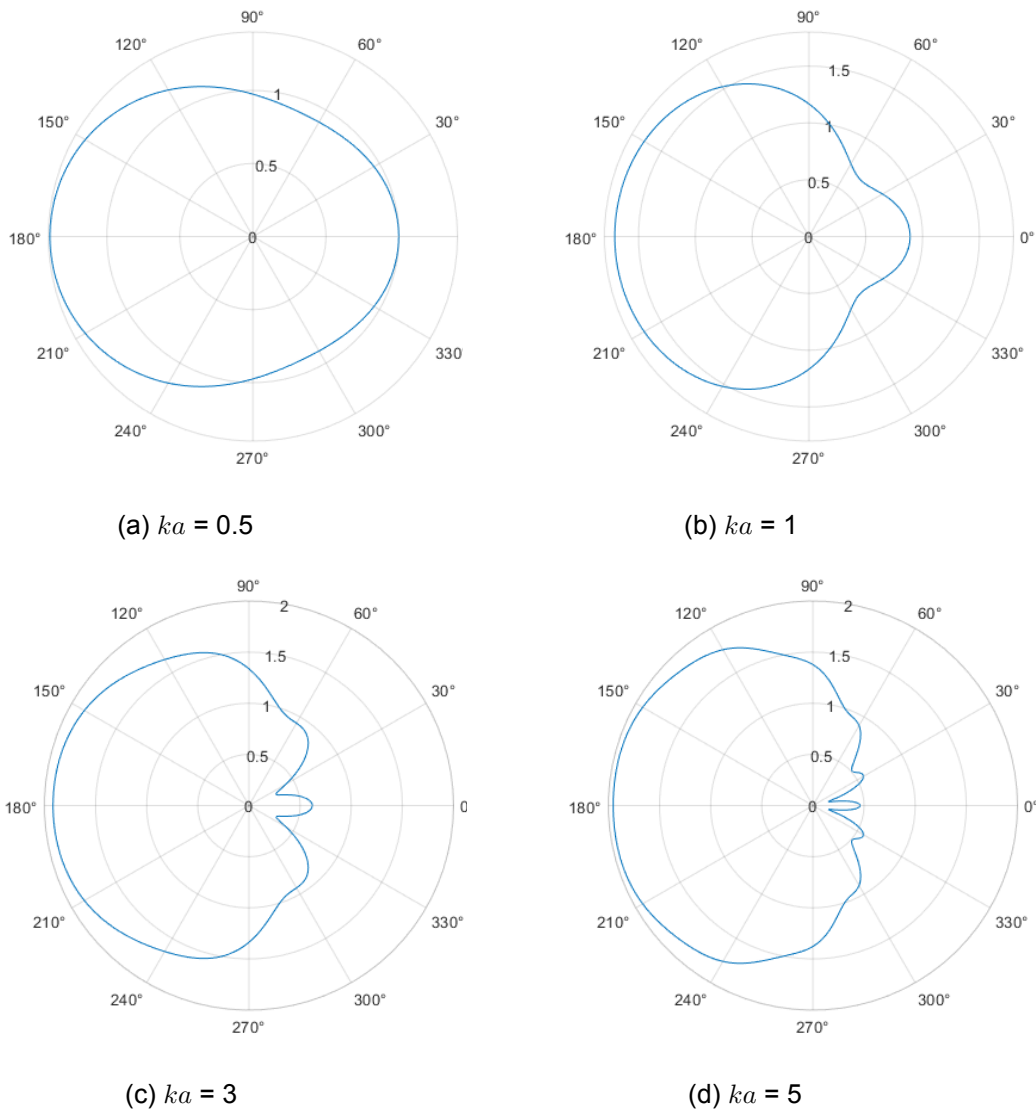

(a) ka = 0.5

(b) ka = 1

(c) ka = 3

(d) ka = 5

Figure 3.4: Run-up around a cylinder for different relative wavelength ka.

It can be noted that for small ka the run-up distribution is mostly even around the cylinder, indicating that long waves are barely disturbed by the presence of the cylinder and thus, there is no shadow effect. Conversely, as ka increases (i.e., shorter waves), the run-up variation gets more complex around the cylinder and the diffraction effects grow.

These plots agree well with [1], Fig. 5.1. Therefore, it can be concluded that the calculation of the analytical solution is valid.

3.2.1 Computational optimization

As Fig. 3.4 shows, it is noted that run-up complexity around the cylinder increases as ka increases. Hence, more terms m in the expansion will be needed in order to achieve

Real-Time Simulation of Service Vessels for Offshore Wind Turbine

10e-6 accuracy threshold on the required calculations, e.g. surface elevation, pressure, forces, etc.

The range of ka established in Section 2.2 considering climate conditions in the studied location, Horns Rev III, will help to determine it. Given the greatest value of the obtained range is $ka = 4$, we can conclude $M = 13$, as shown in the following Figure.
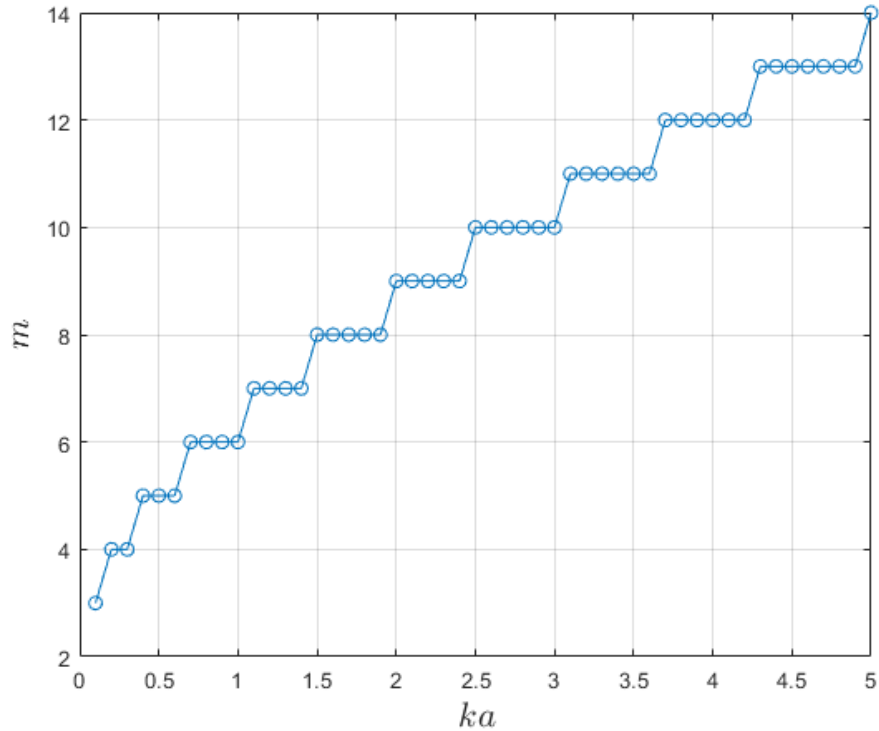

Figure 3.5: Number of iterations m to reach an accuracy threshold of 10^{-6}, M.

3.3 Motions of a ship in regular waves

This section is largely based on [8] and [9], Section 14.

Studying how regular waves of different frequencies impact a ship is the first step needed to be able to predict the statistics of the responses to different seaways, which is the main objective.

The current case consists of evaluating the response of a longitudinally symmetrical ship, with null forward speed, to regular waves coming from $x \sim -\infty$ with different frequencies. As a result, the ship will move in six degrees of freedom and since it has a port/starboard symmetry, it can be assumed that the longitudinal-vertical plane motions, i.e. surge (η_1), heave (η_3) and pitch (η_5) are uncoupled from the transverse-vertical plane motions as sway (η_2), roll (η_4) and yaw (η_6).
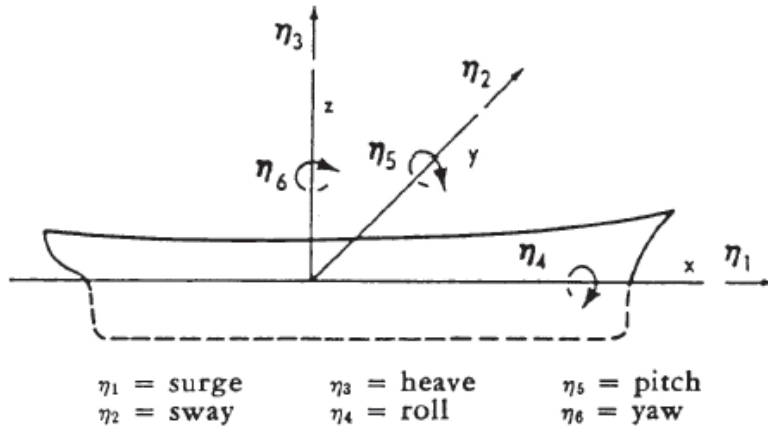
Figure 3.6: Sign convention for fluid forces and moments [9].

The uncoupling results in a reduction in two sets of three linear equations of motion, governed by Newton's 2nd law. The linearization of these equations requires the motions to be generally small, assuming the ship to be stable and the incident wave amplitude relatively small. Therefore, after all transients have decayed to zero, the response of the ship will be also time-harmonic:

$$\eta_j(t) = \Re \left\{ \xi_j(\omega) e^{i\omega t} \right\}, \quad j = 1, 2, ..., 6. \tag{3.24}$$

where $\xi_j(w) = \xi_{j,a} e^{i\epsilon_j}$ is the complex amplitude of the motion. $\xi_{j,a} = |\xi_j|$ is the amplitude motion and ϵ_j is the phase angle, relative to the incident wave elevation at a certain location.

The general form of Newton's second law of the rigid-body motion equations is given by

$$\sum_{j=1}^{6} M_{ij} \, \ddot{\eta}_j(t) = F_i(t), \quad i = 1, 2, ..., 6, \tag{3.25}$$

where M_{ij} are the components of the generalized inertia matrix for the ship, including mass and moment of inertia terms. $\ddot{\eta}_j$ is the acceleration in mode j and F_i corresponds to the total force or moment acting on the body in direction i.

The total Forces on the body can be divided into three different groups: the hydrostatic restoring force F_i^S, hydrodynamic radiation force F_i^R (including added mass and damping forces), and excitation forces F_i^E.

$$M_{ij} \, \ddot{\eta}_j = F_i^S + F_i^R + F_i^E. \tag{3.26}$$

This can be pictured in a different angle, where the motion of the body is the superposition of two states:

1. The structure is restrained from oscillating and there are incident regular waves. The wave excitation loads take place and are composed of so-called F-K and diffraction forces and moments, F_i^E.

2. There are no incident waves but the structure is forced to oscillate with the wave excitation frequency in any rigid-body motion mode. Added mass (A_{ij}) and damping

Real-Time Simulation of Service Vessels for Offshore Wind Turbine

(B_{ij}), and restoring terms (C_{ij}) take place, involved in their corresponding forces, i.e. F_i^R and F_i^S, respectively.

Therefore, we can rearrange the motion equation as follows

$$(M_{ij} + A_{ij})\,\ddot{\eta}_j + B_{ij}\,\dot{\eta}_j + C_{ij}\,\eta_j = \Re\left\{AX_i \mathrm{e}^{\mathrm{i}\omega t}\right\}, \tag{3.27}$$

where $\dot{\eta}_j$ and η_j are the velocity and displacement, respectively, in mode j, A is the amplitude of the incident wave and X_i is the complex amplitude of the wave excitation load due to a regular wave with unit amplitude.

Invoking Eq. (3.24), the body motion equations thus become

$$\Re\left\{\left[-\omega^2(M_{ij} + A_{ij}) + \mathrm{i}\omega B_{ij} + C_{ij}\right]\xi_j(\omega,\theta)\mathrm{e}^{\mathrm{i}\omega t}\right\} = \Re\left\{AX_i(\omega,\theta)\mathrm{e}^{\mathrm{i}\omega t}\right\}, \tag{3.28}$$

and, given that it is valid for any time instant t, it can be also written as

$$\underbrace{\left[-\omega^2\left(M_{ij} + A_{ij}\right) + \mathrm{i}\omega B_{ij} + C_{ij}\right]}_{D_{ij}}\xi_j(\omega,\theta) = AX_i(\omega,\theta). \tag{3.29}$$

Hence, a solution for the complex motion ξ_j is given by

$$\xi_j(\omega,\theta) = D_{ij}^{-1}\,AX_i(\omega,\theta) \tag{3.30}$$

where D_{ij}^{-1} is the inverse of matrix D_{ij}, which can be used to compute the Response Amplitude Operator (RAO). The RAOs are complex functions of wave frequency ω and wave heading angle θ.

$$H_j(\omega,\theta) = \frac{\xi_j}{A} = D_{ij}^{-1}\,X_i(\omega,\theta) \tag{3.31}$$

3.4 Extension to irregular seas

The study of irregular waves is largely based on [10].

As discussed in Section 3.1.1, this document's solutions are based on linear wave theory. That implies the concept of superposition, i.e. any irregular wave can be reproduced as a combination of individual regular waves with different wave frequencies ω_i, wave amplitudes A_i, wave phases ϵ_i and wave numbers k_i. Thus, the wave elevation can be written as

$$\eta(x,t) = \sum_{i=1}^{N} A_i \cos(\omega_i t - k_i \cdot x + \varepsilon_i). \tag{3.32}$$

and the wave amplitude can be expressed in terms of the wave spectra $S(\omega)$

$$A_i = \sqrt{2S(\omega_i)\Delta\omega}. \tag{3.33}$$

Any wave spectra can fully define any wave system, which is responsible for the elevation of a sea surface being a Gaussian process (i.e. negative and positive values of the surface elevation are equally likely) and with wave heights following the Rayleigh distribution (i.e. accounts only for positive values) [9]. For this case, a parameterised wave spectra, i.e. JONSWAP spectrum has been used

$$S_J(\omega) = A_\gamma S_{PM}(\omega) \gamma^{\exp\left(-0.5\left(\frac{\omega - \omega_p}{\sigma \omega_p}\right)^2\right)} \tag{3.34}$$

where:

$\gamma =$ non-dimensional peak shape parameter
$\sigma =$ spectral width parameter
σ_a for $\omega \leq \omega_p$
σ_b for $\omega > \omega_p$
$A_\gamma = 1 - 0.287 \ln(\gamma)$ is a normalizing factor

Average values for the Jonswap experimental data are $\gamma = 3.3, \sigma_a = 0.07, \sigma_b = 0.09$. For $\gamma = 1$, the Jonswap wave spectrum reduces to the PM wave spectrum.

The Jonswap wave spectrum is expected to be a reasonable model for:

$$3.6 < T_p/\sqrt{H_s} < 5$$

Note that this particular spectra depends on the wind speed U_{10}, specifically at a height of $10\,\text{m}$ above the mean sea level, and the fetch F.

The integral wave parameters used are the following:

- Hs = $2\,\text{m}$.

- Tp = $7\,\text{s}$.

These and many other integral wave parameters can be expressed through the n-th order spectral moment, defined by:

$$m_n = \int_0^\infty \omega^n S_\eta(\omega) d\omega. \tag{3.35}$$

It can be noted that the variance of the wave system becomes identical to m_0, equivalently the area under the spectrum. In addition, the zeroth order spectral moment can be related to the average of the 1/3 highest waves in the spectrum by the following equation

$$Hs = 4\sqrt{m_0}. \tag{3.36}$$

Given the previous relations, it is straightforward to obtain the wave spectra (see Fig. 3.8) from the non-dimensional incident irregular wave signal from Fig. 3.7.
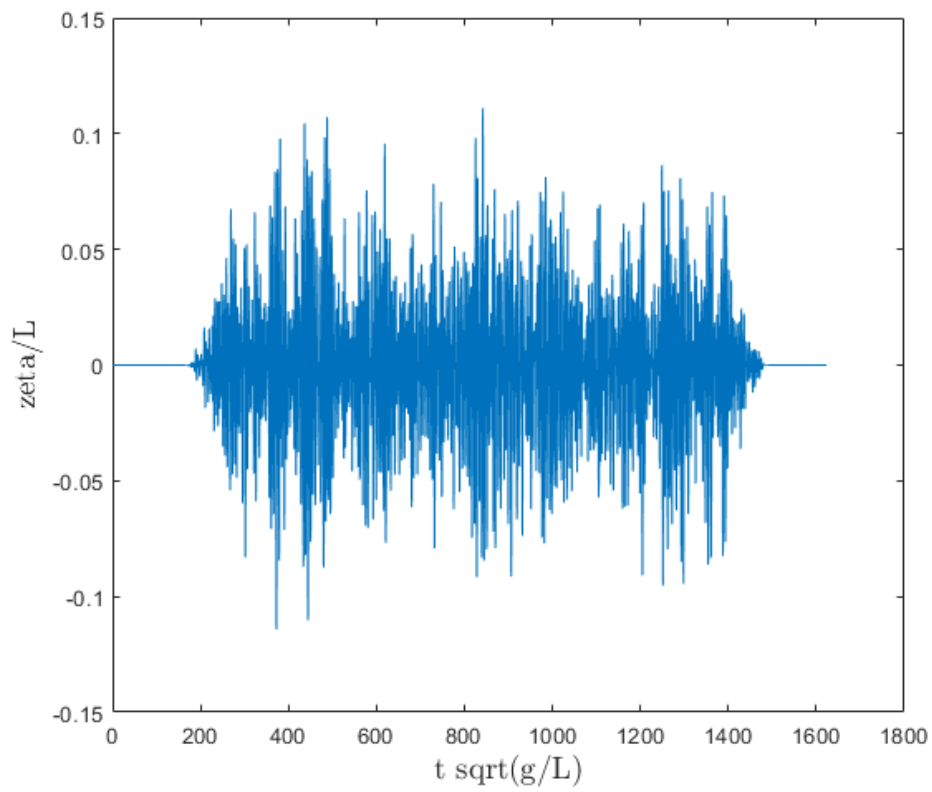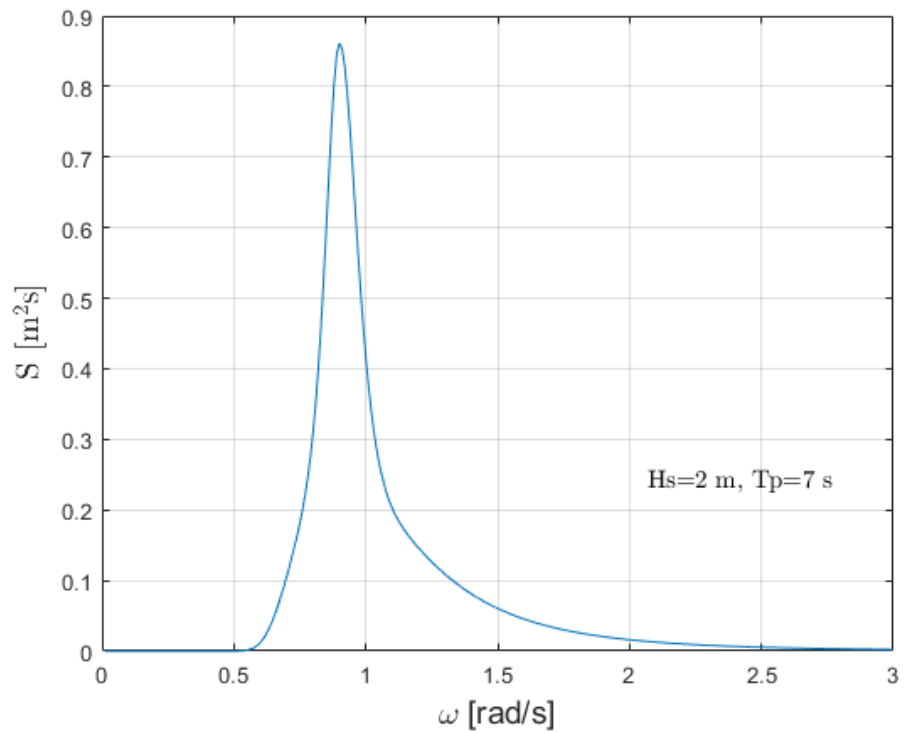
Figure 3.7: Incident wave signal.

Figure 3.8: JONSWAP spectra.

Linear Time-Domain Formulation
Any linear, time-invariant system is fully characterized by its impulse response such that the response to any excitation, by convolution with the Impulse Response Function (IRF), can be known.

Radiation Forces
Invoking Bernoulli's equation and integrating the pressure over the wetted body surface with the generalized normal vector n_j, the radiation forces are obtained

$$
\begin{aligned}
F_j^R &= \int_{S_b} p_k n_j dS \\
&= -\left[a_{jk}^\infty \ddot{x}_k + \int_{-\infty}^t K_{jk}(t-\tau)\dot{x}_k(\tau)d\tau \right]
\end{aligned}
\tag{3.37}
$$

as the combination of an impulsive and memory term, i.e. the true added mass a_{jk}^∞ and the convolution integral, corresponding to the radiation Impulse response Functions (IRFs).

The Impulsive Diffraction Problem
The diffraction, as seen in Section 3.1, is a component of the general solution for linear wave-structure interaction and formed by the combination of the incident wave potential ϕ_0 and the scattered potential ϕ_s (also known as ϕ_7). It thus represents the interaction of the fixed body with an incident wave.

Assuming the incident waves can be represented by a superposition of long-crested impulsive waves, the diffraction IRF is then

$$
K_{jD}(t) = -\rho \int_{S_b} \frac{\partial}{\partial t}\left(\hat{\phi}_0 + \hat{\phi}_7 \right) n_j dS.
\tag{3.38}
$$

and a particular wave exciting forces (measured at the origin of the body coordinate system) is obtained by convolution with the diffraction IRF

$$
F_{jD}(t) = \int_{-\infty}^\infty K_{jD}(t-\tau)\zeta_0(\tau)d\tau.
\tag{3.39}
$$

The Time-Domain Equations of Motion
Combining the radiation and diffraction forces discussed above, with the inertial M_{jk} and hydrostatic C_{jk} loading gives the equations of motion in the time-domain

$$
\left(M_{jk} + A_{jk}^\infty \right) \ddot{x}_k(t) + \int_{-\infty}^t K_{jk}(t-\tau)\dot{x}_k(\tau)d\tau + C_{jk}x_k(t) = F_{jD}(t)
\tag{3.40}
$$

where a sum over repeated indices k is implied.
Since the IRF's and FRF's are Fourier transform pairs, the time- and frequency-domain formulations are equivalent:

Real-Time Simulation of Service Vessels for Offshore Wind Turbine

$$A_{jk}(\omega) = A_{jk}^\infty - \frac{1}{\omega} \int_0^\infty K_{jk}(t) \sin \omega t dt \qquad (3.41a)$$

$$B_{jk}(\omega) = \int_0^\infty K_{jk}(t) \cos \omega t dt \qquad (3.41b)$$

$$X_j(\omega) = \int_{-\infty}^\infty K_{jD}(t) e^{-i\omega t} dt \qquad (3.41c)$$

and

$$K_{jk}(t) = -\frac{2}{\pi} \int_0^\infty \omega \left(A_{jk}(\omega) - A_{jk}^\infty \right) \sin \omega t d\omega = \frac{2}{\pi} \int_0^\infty B_{jk}(\omega) \cos \omega t d\omega \qquad (3.42a)$$

$$K_{jD}(t) = \frac{1}{2\pi} \int_{-\infty}^\infty X_j(\omega) e^{i\omega t} d\omega. \qquad (3.42b)$$

4 Numerical Methods

4.1 Closed form validation case

This section aims to validate the procedure used to evaluate Eq. (3.22) and predict the force on a nearby structure influenced by the scattered wave field due to the cylinder. Hence, a bottom-mounted plate will be considered at a distance $r = d$ from the cylinder, representing an arc with radius d, from θ_1 to θ_2, as depicted in Fig. 4.1.
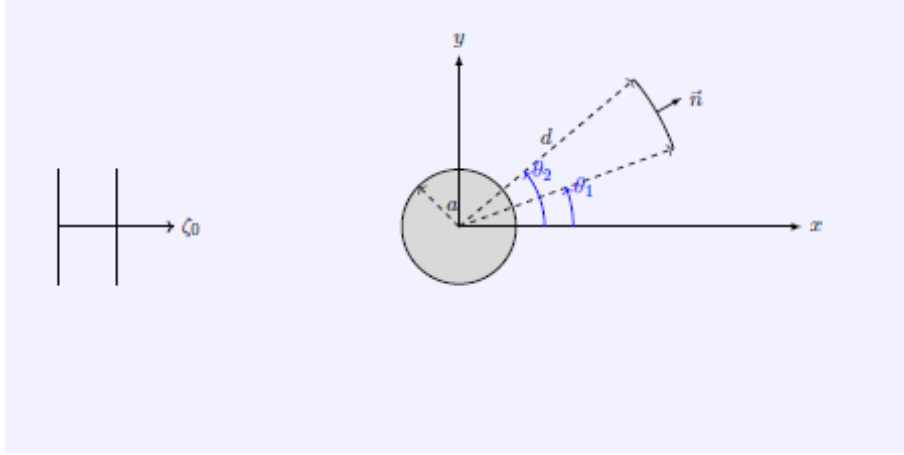
Figure 4.1: Layout of cylinder and bottom-mounted plate used for forces validation [7].

Following [7], the force on the arc can be written in closed form. With the unit normal vector to the plate given as $\vec{n} = [\cos\theta, \sin\theta, 0]$ and, inserting Eq. (3.21) into Eq. (3.22), the force due to the scattered wave field in the x-direction yields

$$F_1^s = \rho g A \int_{-h}^{0} \int_{\theta_1}^{\theta_2} \frac{\cosh[k(z+h)]}{\cosh kh} \sum_{m=0}^{\infty} \epsilon_m(-\mathrm{i})^m \frac{J_m'(ka)}{H_m'(ka)} H_m^{(2)}(kd) \cos m\theta \cos\theta \, d\theta \, dz$$

$$\frac{F_1^s}{\rho g A h d} = \frac{\tanh kh}{kh} \sum_{m=0}^{\infty} \epsilon_m(-\mathrm{i})^m \frac{J_m'(ka)}{H_m'(ka)} H_m^{(2)}(kd)$$

$$\frac{1}{m^2-1} \left(\cos m\theta_1 \sin\theta_1 - m\cos\theta_1 \sin m\theta_1 - \cos m\theta_2 \sin\theta_2 + m\cos\theta_2 \sin m\theta_2 \right).$$

$$(4.1)$$

It can be noted that the trigonometric expression needs to be defined for $m = 1$. By setting $m = 0$ and taking the limit as $m \to 1$ the first two terms can be computed from

$$\sin\theta_2 - \sin\theta_1, \quad m = 0 \tag{4.2}$$

$$\frac{1}{2}\left(\theta_2 - \theta_1 + \cos\theta_2 \sin\theta_2 - \cos\theta_1 \sin\theta_1\right), \quad m = 1. \tag{4.3}$$

Furthermore, replacing the Bessel Functions in Eq. (4.1) by J_m gives the Froude-Krylov force (F-K) on the plate in the x-direction, i.e. F_1^0, as seen in the following equation:

$$-J_m(kd) \rightarrow \frac{J'_m(ka)}{H_m^{(2)'}(ka)} H_m^{(2)}(kd)$$ (4.4)

A comparison of both non-dimensional forces, i.e. F-K and scattered forces, acting on a plate of 40º with $h/a = 4$ and $d/a = 2$, is depicted in Fig. 4.2. The left-hand figure corresponds to an arc placed in front of the cylinder which could be deduced since there is an increase in the total force on the plate due to the scattered force contribution for long waves. It can also be noted the diffraction effects giving an oscillation of the total force as waves get shorter, vanishing as wavelength approaches 0. Conversely, when the arc is placed behind the cylinder, the scattered wave field dampens the resultant force on the plate for all wavelengths, due to the sheltering effect.

(a) Arc in front of the cylinder. (b) Arc behind the cylinder.
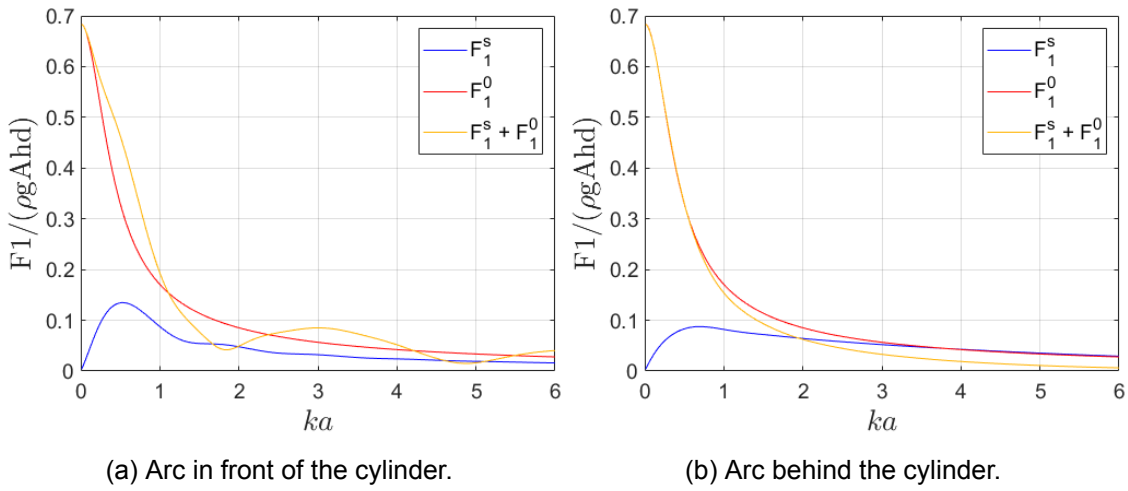
Figure 4.2: Comparison of forces changing the position of the arc around the cylinder.

4.1.1 BEM validation

Previously, in Section 4.1, an exact solution was worked out to compute the forces on a 40º arc bottom mounted near the cylinder. While This is a closed-form solution that cannot be generalized, this section will apply a low-order panel method over a same structure where the pressure will be assumed constant (equal to the value at the centroid) on each flat panel that approximates the structure. Thus,

$$F_i = \sum_{j=1}^{N} p_j \, n_i \, s_j, \quad i = 1, 2, ..., 6,$$ (4.5)

where p_j is the pressure at each panel centroid j, n_i the unit normal vector to the panel in the i direction, and S_j, the area of panel j.

This method considers the aforementioned arc discretized using a collection of N flat panels defined by four vertices, as shown in Fig. 4.3, which are defined in the local body coordinate system centred at the centre of the arc (i.e. centroid) with the x-axis along the arc radius.
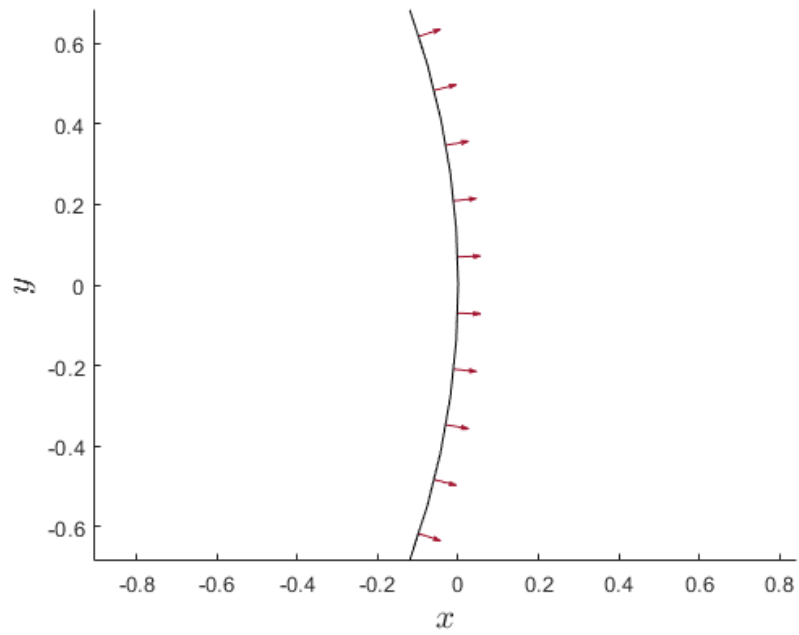
Figure 4.3: Example of panel geometry, top view. N=200.

A comparison of the forces obtained by the exact solution from Eqs. (4.1) and (4.4), and the one computed with the panel method can be seen in Fig. 4.4, where the difference between them is depicted (i.e. error). Both forces, i.e. scattered and F-K follow a similar error profile, where the error of the real part increases exponentially as ka increases, i.e. as waves get shorter although the imaginary part remains close to 0. In addition, as the number of panels N increases, it is noticeable how the error converges to 0 for all ranges of ka. Therefore, we can conclude the panel method implementation in MATLAB is valid.
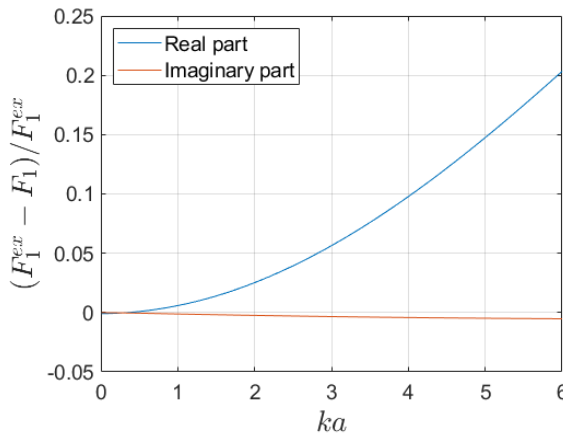
(a) Scattered force comparison, N=100.
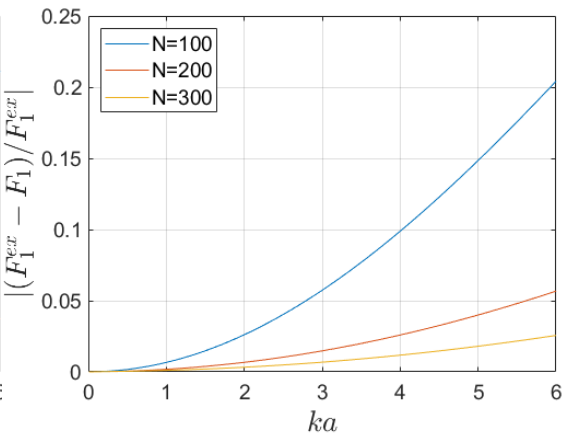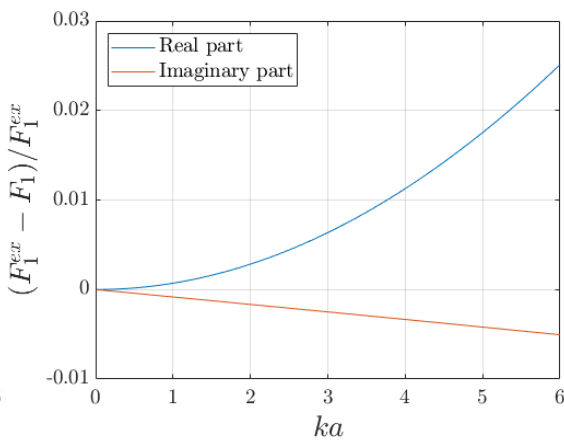
(b) F-K comparison, N=100.
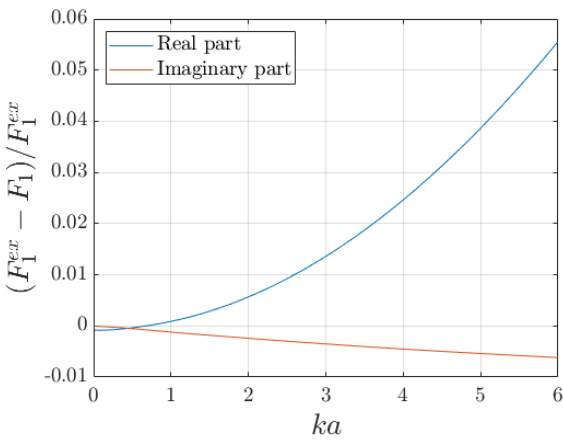
(c) Scattered force comparison, N=200.
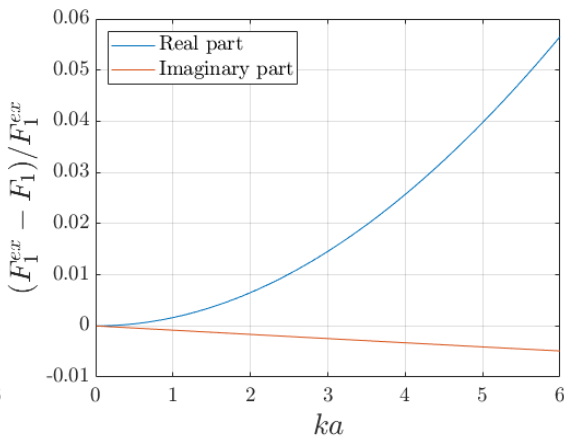
(d) F-K comparison, N=200.
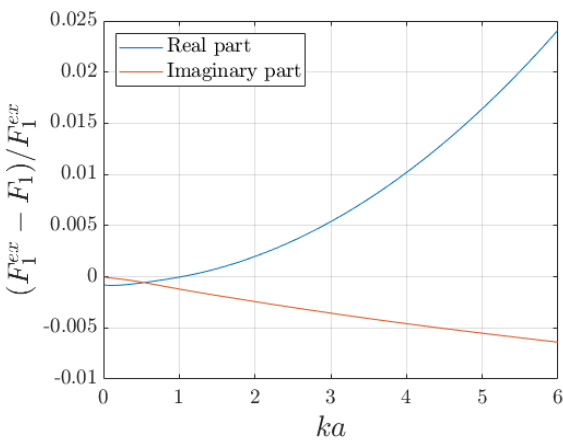
(e) Scattered force comparison, N=300.

(f) F-K force comparison, N=300.

Figure 4.4: Convergence of BEM method changing number of panels.

Lastly, the following figure depicts an overview of the absolute relative error when varying the number of panels; concluding then, that a greater number of panels is needed when calculating the forces for greater values of ka.
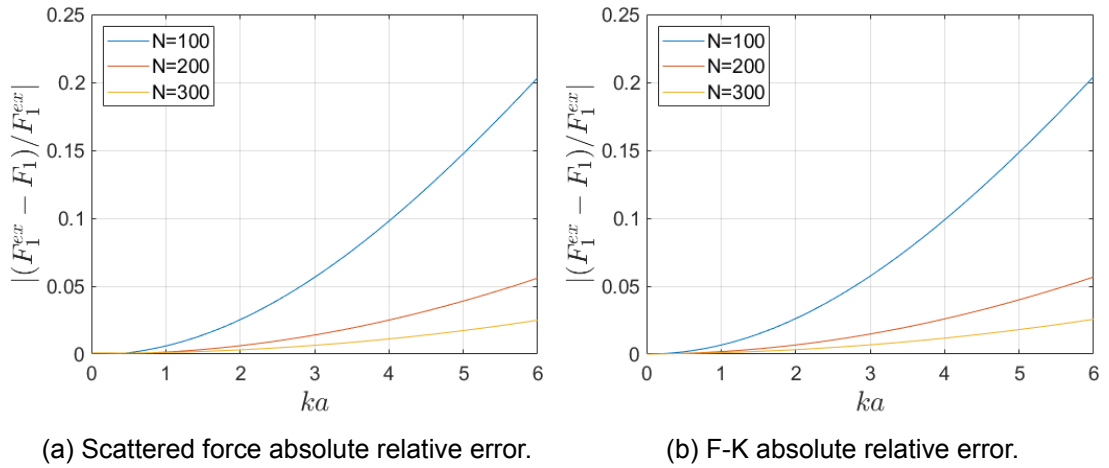
(a) Scattered force absolute relative error.   (b) F-K absolute relative error.

Figure 4.5: Convergence of BEM method.

4.2 DTU Motion Simulator

DTUMotionSimulator is a Matlab package, available from girlab.gbar.dtu.dk, for simulating the linear response of a marine structure to ocean waves. Therefore, the equations of motions need to be solve in the time-domain in order to simulate the interaction of a structure with a prescribed ocean wave elevation time-series (described in Section 3.4), specified at the origin of the body coordinates.

The convolution can be avoided when calculating the wave exciting force if computed in the frequency-domain. For each incident wave heading angle, a Fast Fourier Transform (FFT) is performed to the incident wave elevation, moved to the body coordinate origin, multiplied by the diffraction FRF and accumulated in the frequency domain. Then, an Inverse FFT is needed to get the time-domain forcing.

$$F_{jD}(t) = \int_{-\infty}^{\infty} K_{jD}(t-\tau)\zeta_0(\tau)d\tau = \text{IFFT}\left\{X_j(\omega)c_0(\omega)\right\} \tag{4.6}$$

where $X_j(\omega) = \text{FFT}\left\{K_{jD}(t)\right\}$ and $c_0(\omega)$ = FFT $\left\{\eta_0(t)\right\}$.

Conversely, the radiation force is computed in the time-domain via the trapezoid rule. There is an interval where the IRF is non-zero $0 \le t \le t_{lim}$ and $x(t)$ is non-zero over the range $0 \le x(t) \le t_m$ where $t_m = m\Delta t$, for $m = 0, 1, ..., M$ total time steps. The range of integration is therefore $t_s \le \tau \le t$ where $t_s = \text{max}(0, t_m - t_{lim})$, or discretely $m_0 = t_s/\Delta t$. Eq. (4.7) shows the convolution integral for the radiation forces at time-step m:

$$\int_{t_s}^{t_m} K(t-\tau)\dot{x}(\tau)d\tau \approx \Delta t \left[\frac{1}{2}\left(K_0\dot{x}_m + K_{m-m_0}\dot{x}_{m_0}\right) + \sum_{n=m_0+1}^{m-1} K_{m-n}\dot{x}_n\right] \tag{4.7}$$

where $K_n = K(n\Delta t)$ and $\dot{x}_n = \dot{X}(n\Delta t)$.

Then it is possible to avoid second-order ODE and reduce the system to a first-order ODE in time by considering the extended vector of velocities and positions: $[\dot{x}_k; x_k]$, $k = 1, 2, ..., 6$

$$\frac{d}{dt}\begin{bmatrix} \dot{x}_j \\ x_j \end{bmatrix} = \begin{bmatrix} M_{jk}^{-1}\left(R_{jk}\dot{x}_j + F_{jD} + F_{jNL}\right) \\ \dot{x}_j \end{bmatrix} \quad (4.8)$$

where R_{kj} contains all the radiation and hydrostatic contributions from past time-steps, while M_{jk} hold all contributions from the current step and F_{jD} and F_{jNL} correspond to the diffraction exciting force and nonlinear external force vectors, respectively. Finally, a solution is reached by integrating the equations forward in time using the classical explicit Runge-Kutta (4,4) scheme.

Finally, the RAOs for every motion can be computed as the ratio of the FFT of the motions, i.e. the vector of velocities and positions, to the FFT of the incident wave elevation

$$\mid \xi_k \mid = \mathsf{FFT}\left\{[\ddot{x}_k; x_k]^{-1}\right\}\mathsf{FFT}\left\{\eta_0(t)\right\}, \qquad k = 1, 2, ..., 6. \quad (4.9)$$

5 Results

5.1 Wigley hull

The Wigley hull is mathematically defined and frequently used to perform validation work and tests. For the current case, the following dimensions are utilised, [11]:

- L/B: 10

- L/T: 16

- Length: $11.5\,\text{m}$

- Wigley Hull equation: $y = \pm\frac{B}{2}\left[1 - \left(\frac{2x}{L}\right)^2\right]\left[1 - \left(\frac{z}{T}\right)^2\right]$

.

The dimensions are chosen to roughly model the boat shown in Fig. 5.1, which is designed to transport personnel safely and quickly to and from wind farms.

Figure 5.1: 3D design of a typical workboat [11].

With WAMIT, it is possible to calculate the hydrodynamic coefficients from a given geometry. In this case, a Wigley hull is generated by flat panels with the mentioned dimensions (see the following figure).
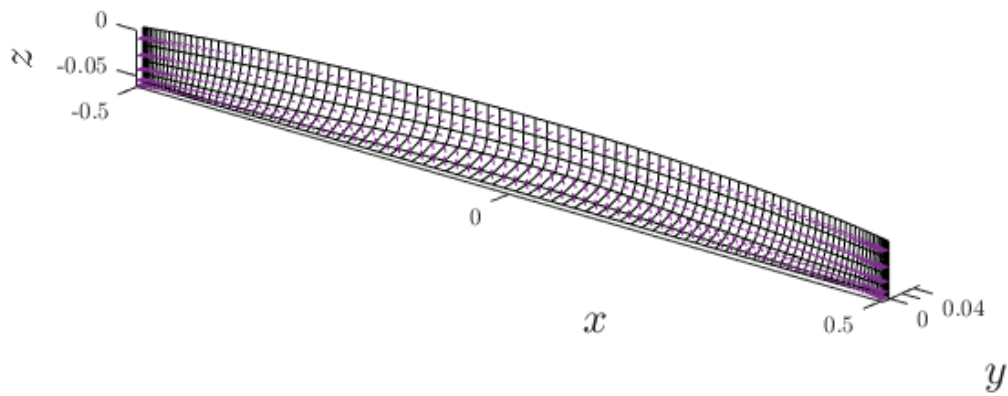
Figure 5.2: Wigley hull flat panel discretization.

Eq. (3.31) has been used to plot the following figures, from 5.4 to 5.7. They represent the RAOs for different approaching angles β of the ship with respect to the cylinder with incoming regular waves from $x \sim -\infty$. In addition, the contribution of the scattered wave field from the cylinder to the RAOs can be observed for all modes of motion (orange line).

Fig. 5.3 depicts the different approaching angles of the ship to the cylinder where the RAO has been evaluated. It should be mentioned that the ships sketched do not belong to this section but to 5.2, since the main purpose of this figure is to show the heading angles β studied.
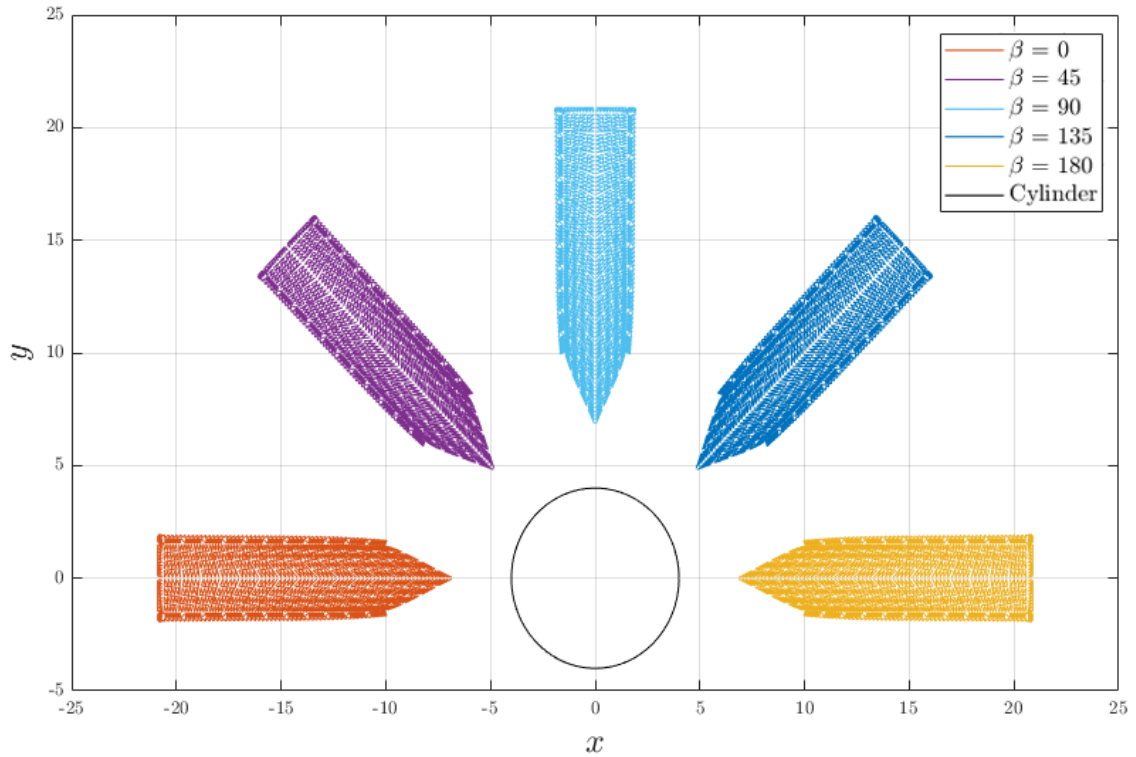
Figure 5.3: Ship approaching angles β.

To begin with, the RAO due to placing the ship in front and behind the cylinder is depicted in Fig. 5.4. It can be noted that the transverse-vertical plane motions have been disregarded since they are negligible (perpendicular to the incoming wave). Hence, only the longitudinal-vertical plane motions, i.e. surge (ξ_1), heave (ξ_3) and pitch (ξ_5) are analysed. The results show what was expected beforehand: the scattered wave field due to the cylinder decreases the RAO in the shadow zone for essentially medium-long range waves.
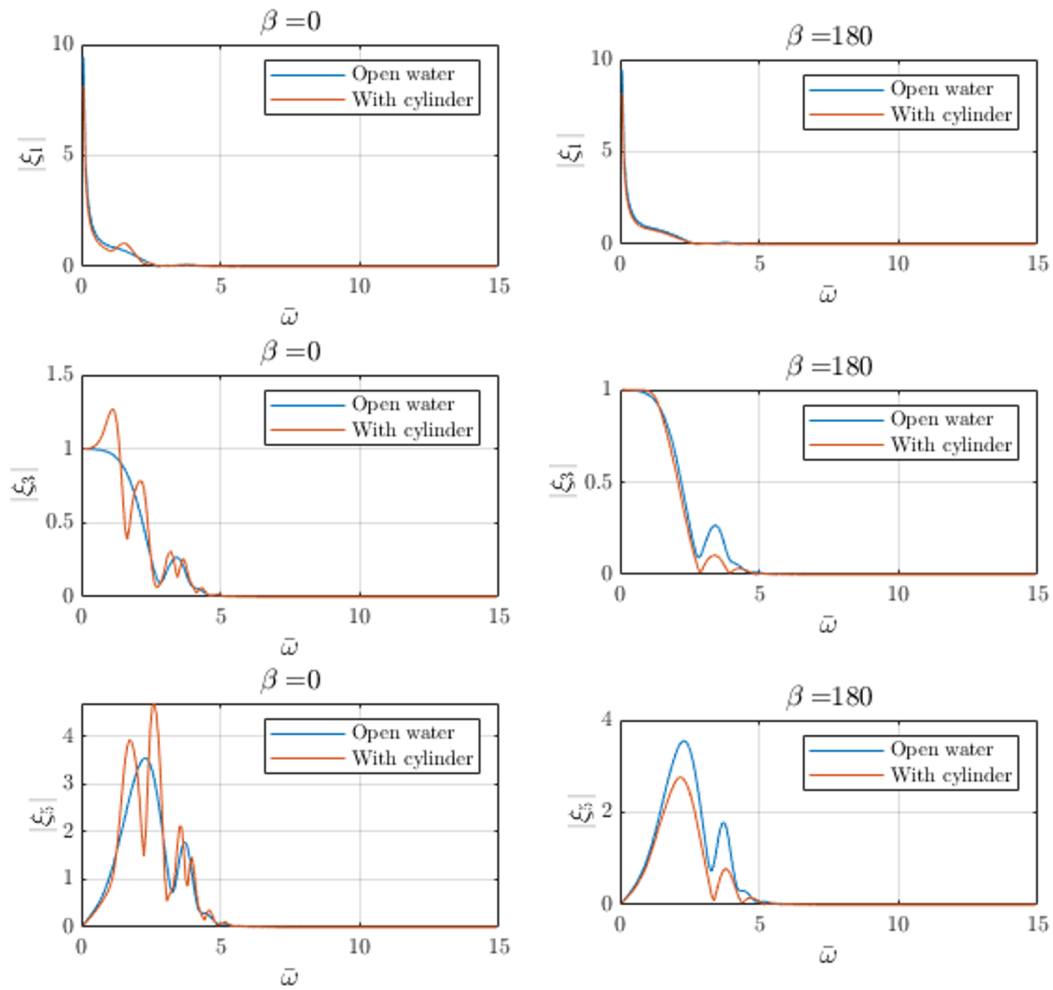
Figure 5.4: RAO for ship located in front and behind the cylinder.

It is known from Eq. (3.27) that when $\omega \to 0$ the vertical motions are dominated by the hydrostatic restoring spring term. This is reflected in the low-frequency area of the RAO, where the the ship tends to "follow" the waves; thus, the RAO tends to 1 for Heave (ξ_3). Physically, at very low frequencies, the wavelength is large compared to the horizontal length of the ship and it will "follow" the waves.

Conversely, under the situation of low-period waves approaching, the ship's response is no longer dependent on the incoming waves since vertical motions are then dominated by the mass term; the wavelengths are too short compared to the dimensions of the ship. This can be observed on every RAO for every mode: RAO~ 0 when $\omega \to \infty$.

Figs. 5.5 and 5.6 show RAO for longitudinal-vertical and transverse-vertical motions, respectively, when the ship is shifted to half the first and second quadrants ($\beta = 45$ and $\beta = 135$). Contrarily to Fig. 5.4, every body motion is considered in this case since there is no longer a motion (see 3.6) perpendicular to the incoming wave.

Regarding the RAO magnitude, it can be noted that every motion in Fig. 5.5 is smaller (especially the surge, reduced by roughly half) compared with Fig. 5.4 since the ship is

Real-Time Simulation of Service Vessels for Offshore Wind Turbine

no longer parallel to the incoming wave. On the other hand, transverse-vertical motions in Fig. 5.6, seem to increase their response as β approaches $90º$.

On top of that, given this ratio, $L/B = 10$, the dimensions of the ship play an important role in the RAO for different heading angles. That is, transverse-vertical plane motions, due to length similarity with the incoming wave, have a greater response to shorter waves compared to longitudinal-vertical plane motions.

When comparing the influence of the cylinder on the RAO to the open water in Fig. 5.5, it is worth mentioning the response amplitude due to the scattered wave field is less fluctuating for longitudinal-vertical motions when the ship is placed for $\beta > 90º$. Nonetheless, the scattered wave field makes no additional impact on the RAO on the transverse-vertical motions in Fig. 5.6.
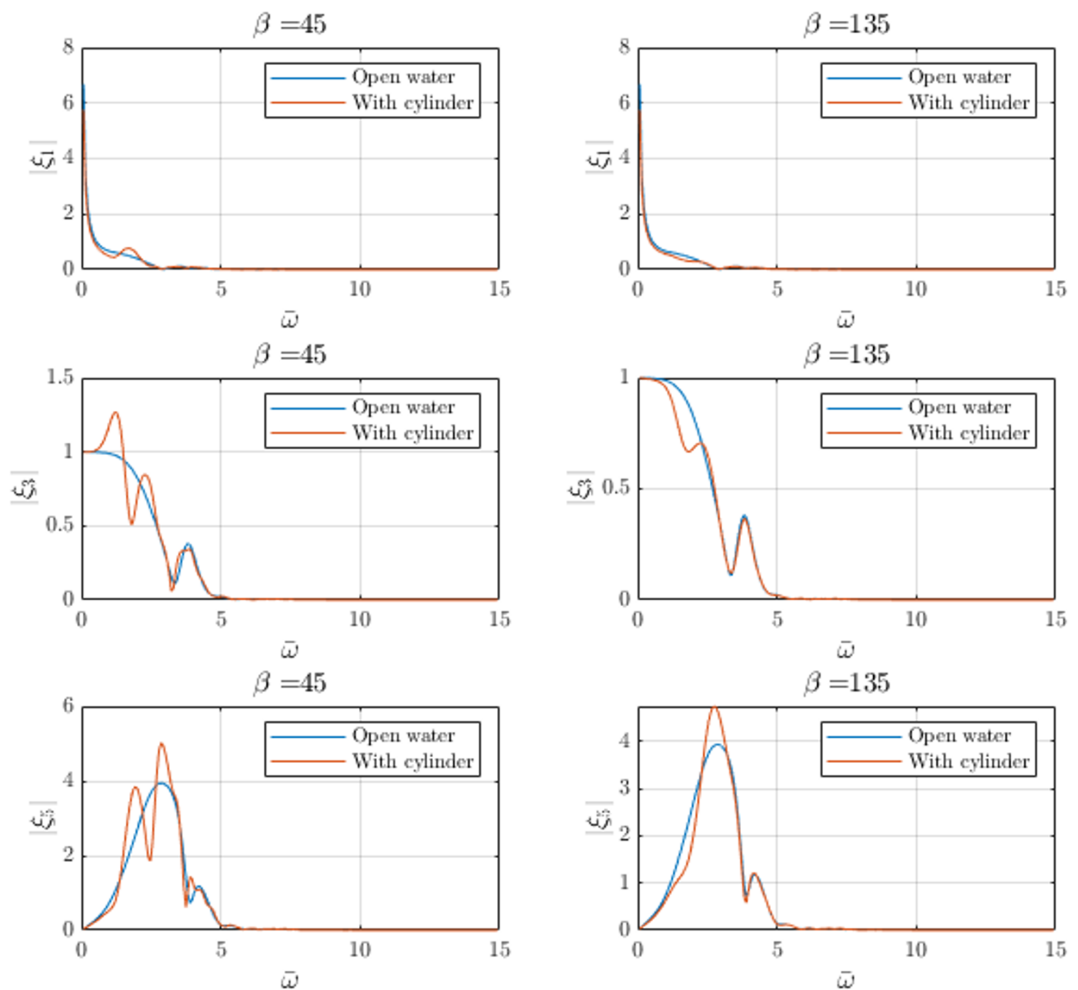
Figure 5.5: Longitudinal-vertical plane RAO for $\beta = 45$ and $\beta = 135$.
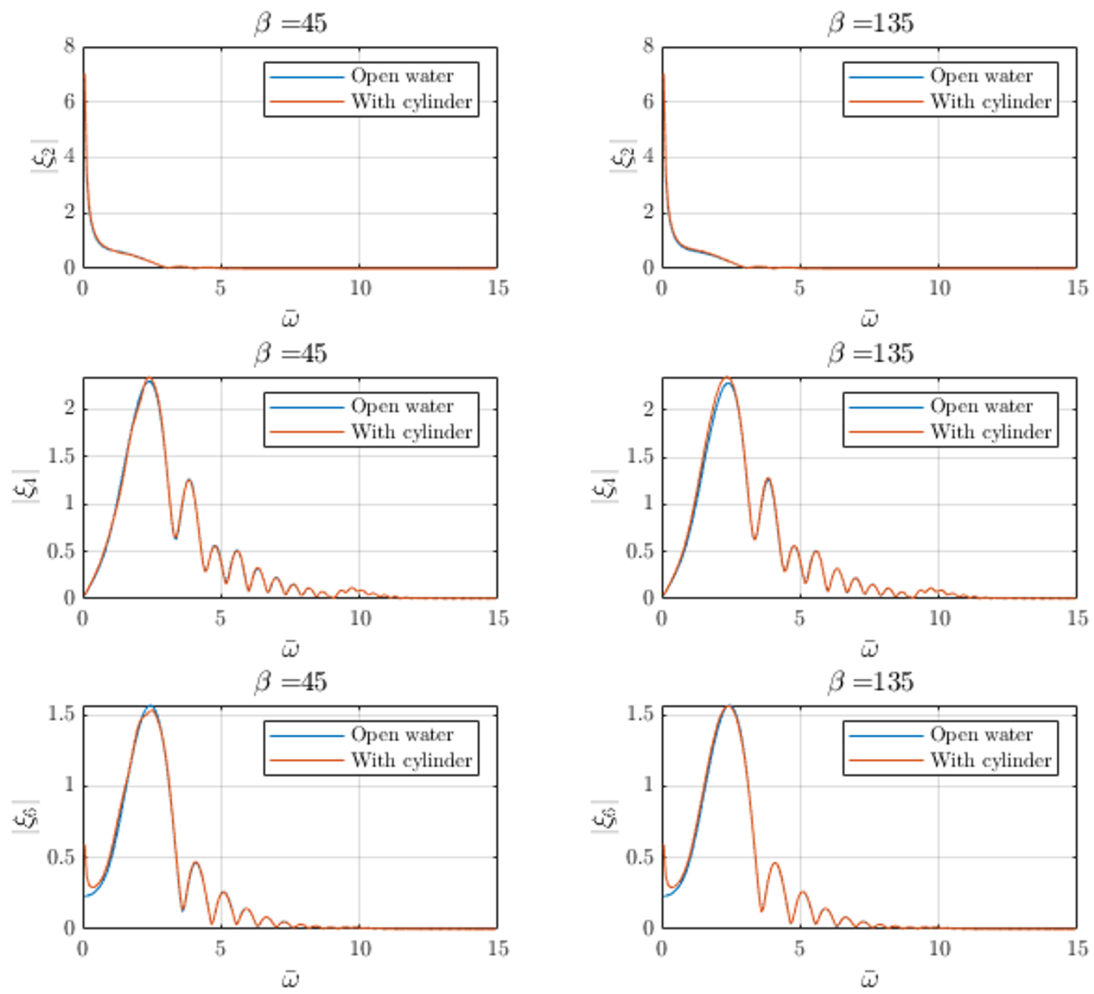
Figure 5.6: Transverse-vertical plane RAO for $\beta = 45$ and $\beta = 135$.

In this case, longitudinal-vertical plane motions of the ship are perpendicular to the incoming wave; hence, negligible (ξ_1 and ξ_5). However, the scattered wave field impact on both is remarkable. In this position, as expected, Sway and Roll are the most affected motions on the body although there is no difference in the RAO when considering the scattered wave field. As mentioned before, a short beam induces the transverse motions to be affected by shorter waves, hence, RAOs cover greater ω.
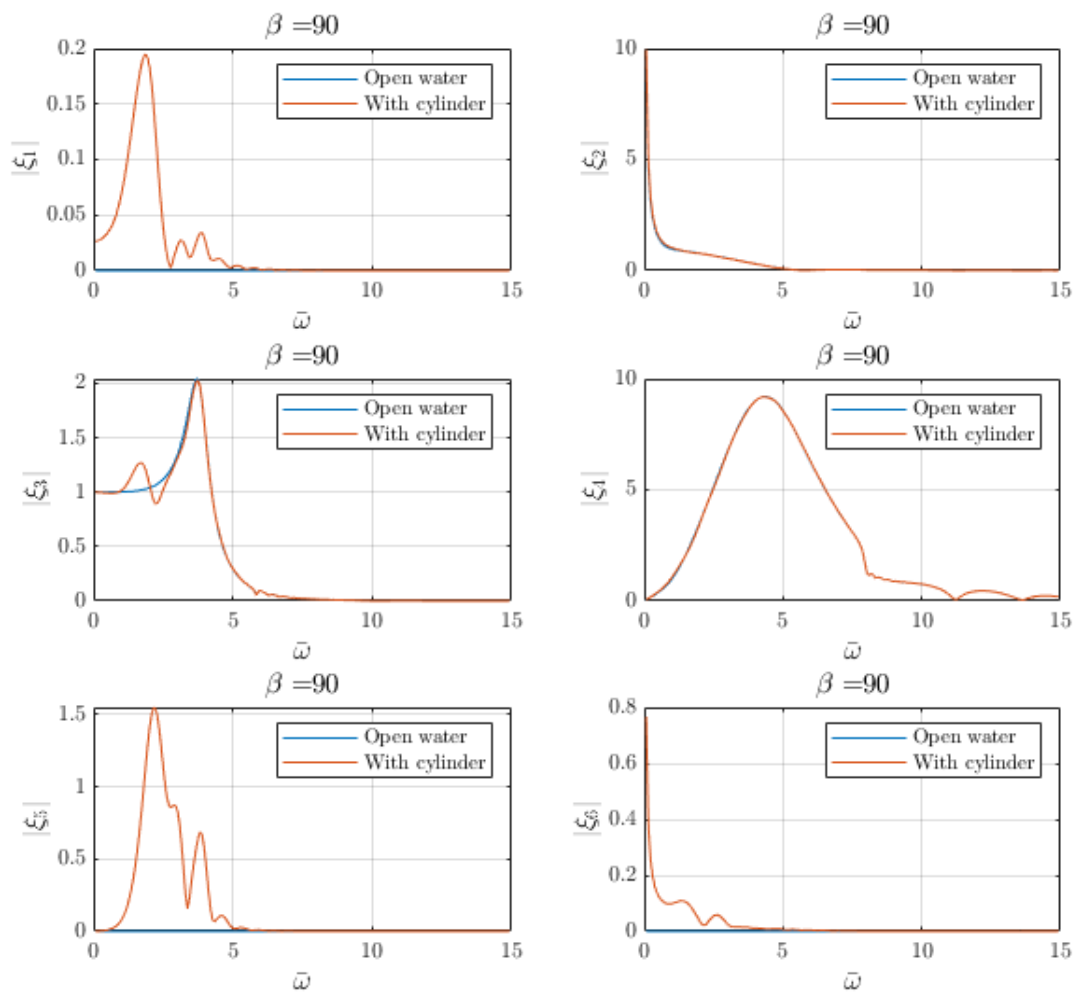
Figure 5.7: RAO for ship located 90º with respect to the incident wave.

5.2 Concept Hull

This section presents a similar analysis as done in 5.1 using a typical workboat. Fig. 5.8 shows the flat panel version geometry of the ship hull. The dimensions used for the analysis are the following:

- Length: $15\,\mathrm{m}$

- Depth: $26\,\mathrm{m}$

- Distance to the cylinder: $15\,\mathrm{m}$

This workboat was designed by Steffan Brandt Tolboe in his BEng project and kindly made available to us in this project.
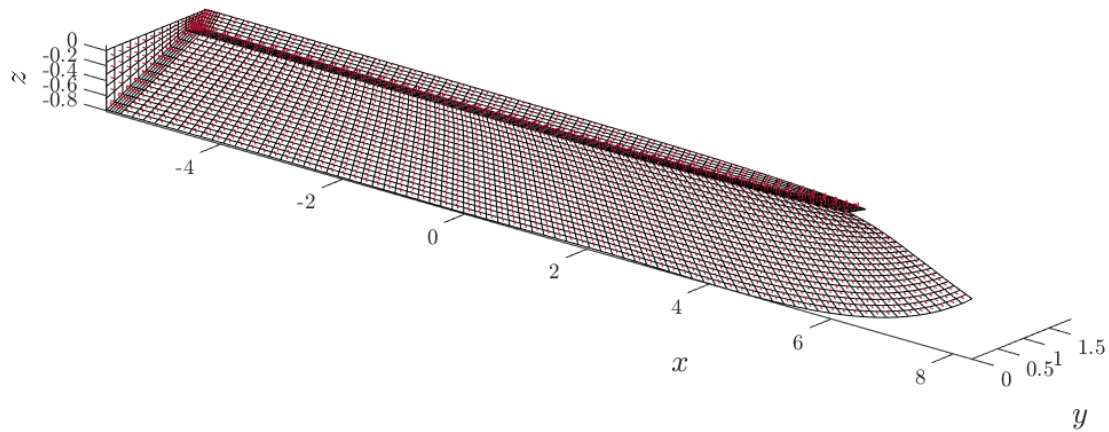
Figure 5.8: Hull design. *Author: Steffan Brandt Tolboe.*

Once the geometry is generated and introduced to WAMIT, hydrodynamic coefficients can thus be calculated and then the RAO, Figs 5.9 to 5.12; where the same pattern of analysis has been followed: first, a comparison of the longitudinal motions response for $\beta = 0$; secondly, analysis of every motion response and comparison of $\beta = 45$ and $\beta = 135$ and lastly; RAO for $\beta = 90$. Expectedly, similar results are obtained regarding the impact of the scattered wave field.

Firstly, Fig. 5.9 shows no additional valuable information to its analogous from the Wigley Hull case: similar RAO for both open water and considering the scattered wave field for every mode but the Surge which is now significantly reduced.

Secondly, regarding Figs. 5.10 to 5.12, only when the ship is placed in $\beta = 90$ (Fig. 5.12), the influence of the cylinder becomes noticeable for essentially ξ_1 and ξ_5 since both are aligned with the reflected waves from the cylinder.

It can be concluded then, by agreeing that the most influenced position of the ship by the cylinder is the one with a heading angle $\beta = 90\,°$.

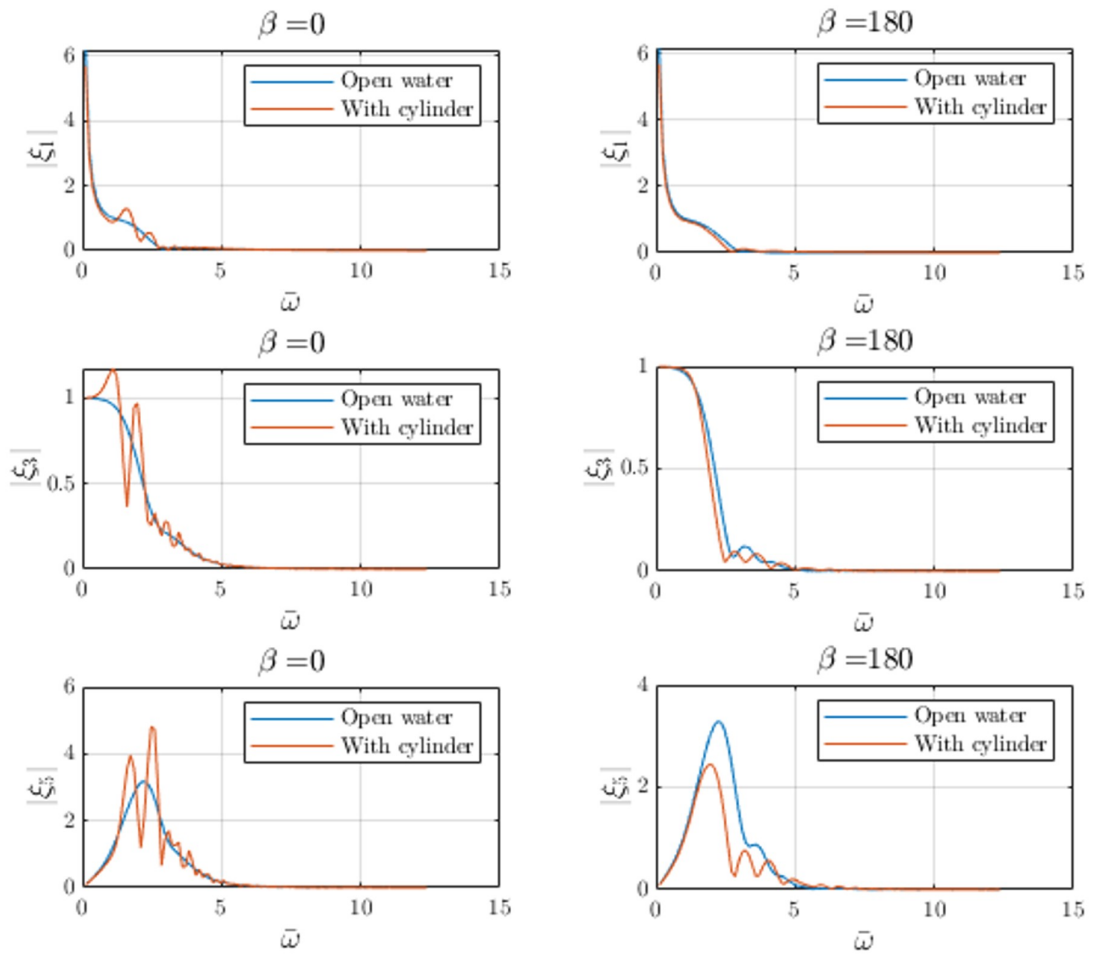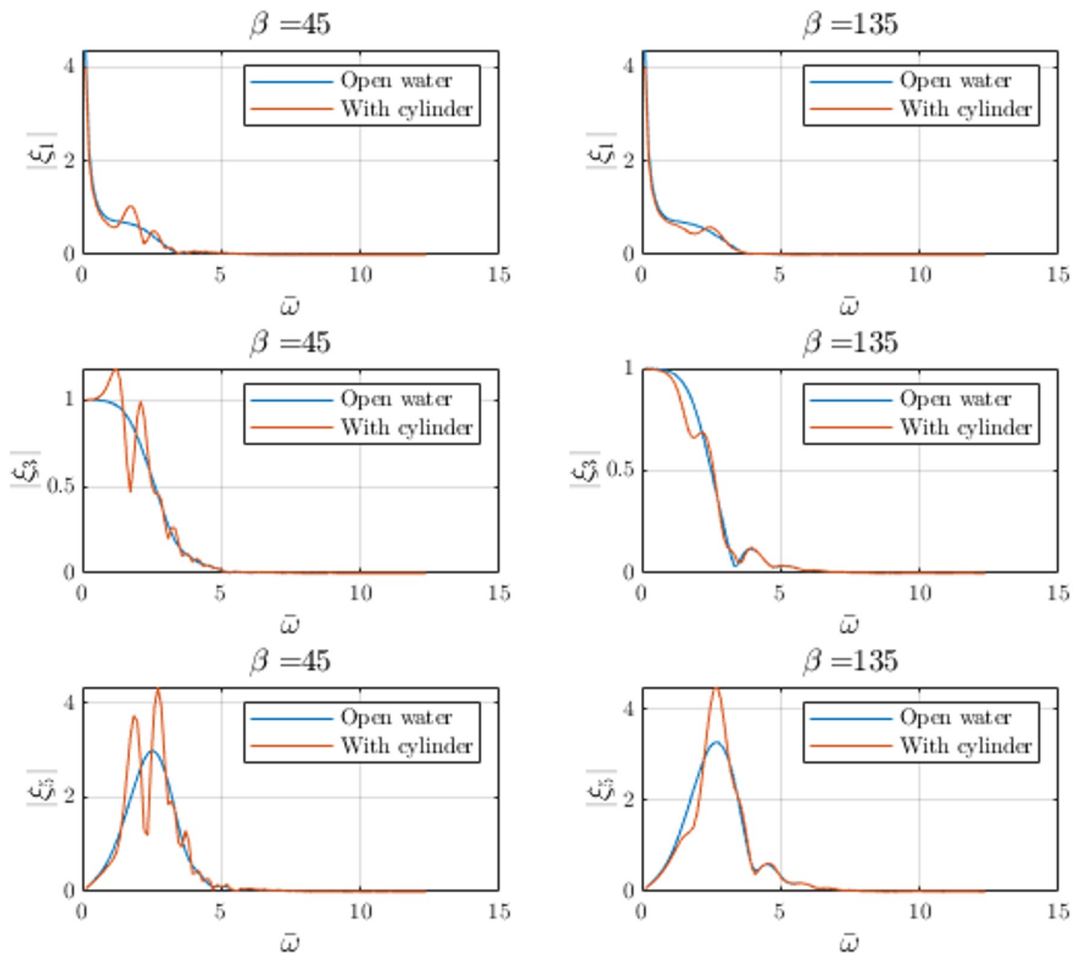Figure 5.9: RAO for ship located in front and behind the cylinder.

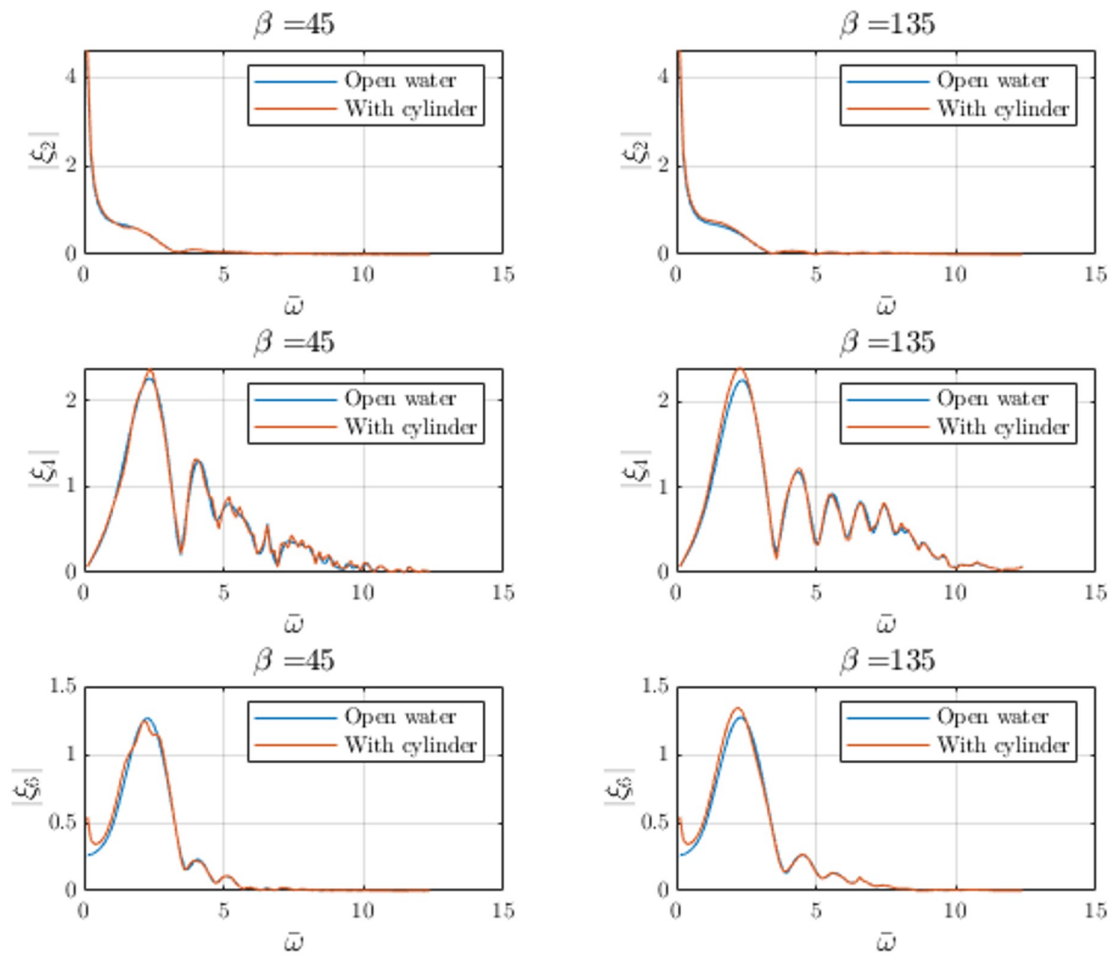Figure 5.10: Longitudinal-vertical plane RAO for $\beta = 45$ and $\beta = 135$.

Real-Time Simulation of Service Vessels for Offshore Wind Turbine

Figure 5.11: Transverse-vertical plane RAO for $\beta = 45$ and $\beta = 135$.
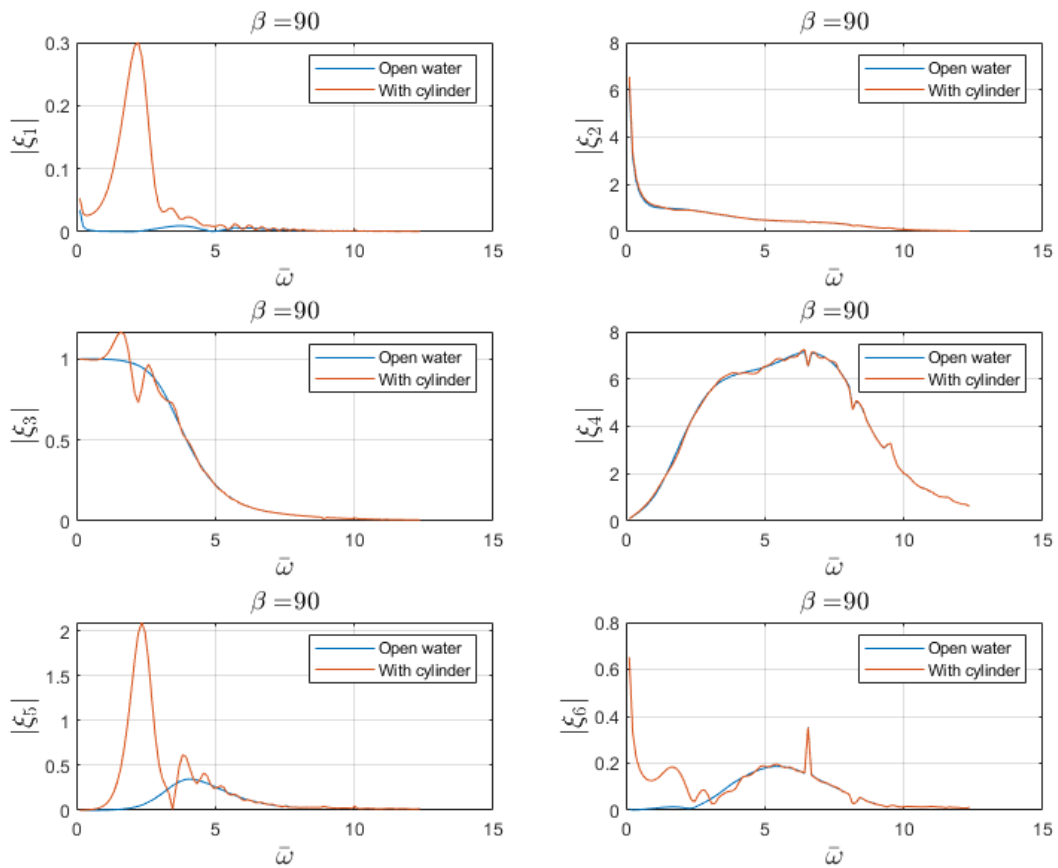
Figure 5.12: RAO for ship located 90º with respect to the incident wave.

5.2.1 Ship motions under irregular waves

Similarly to the analysis of the regular wave, RAOs for different heading angles are shown in the following figures (Figs. 5.13 to 5.16) with the x-axis measured in Hz. These plots are the result of the DTUMotionSimulator package, where the JONSWAP spectrum of $Hs = 2$m and $Tp = 7$s and the scattering contribution from the cylinder have been included. Working out the equations of motion in the time domain by using RK-(4,4) and applying Eq. (4.9). As expected, because of linear superposition, RAO due to regular waves shows no difference from RAO due to irregular waves besides some present perturbations essentially for frequencies close to 0 Hz and greater than 1 Hz.
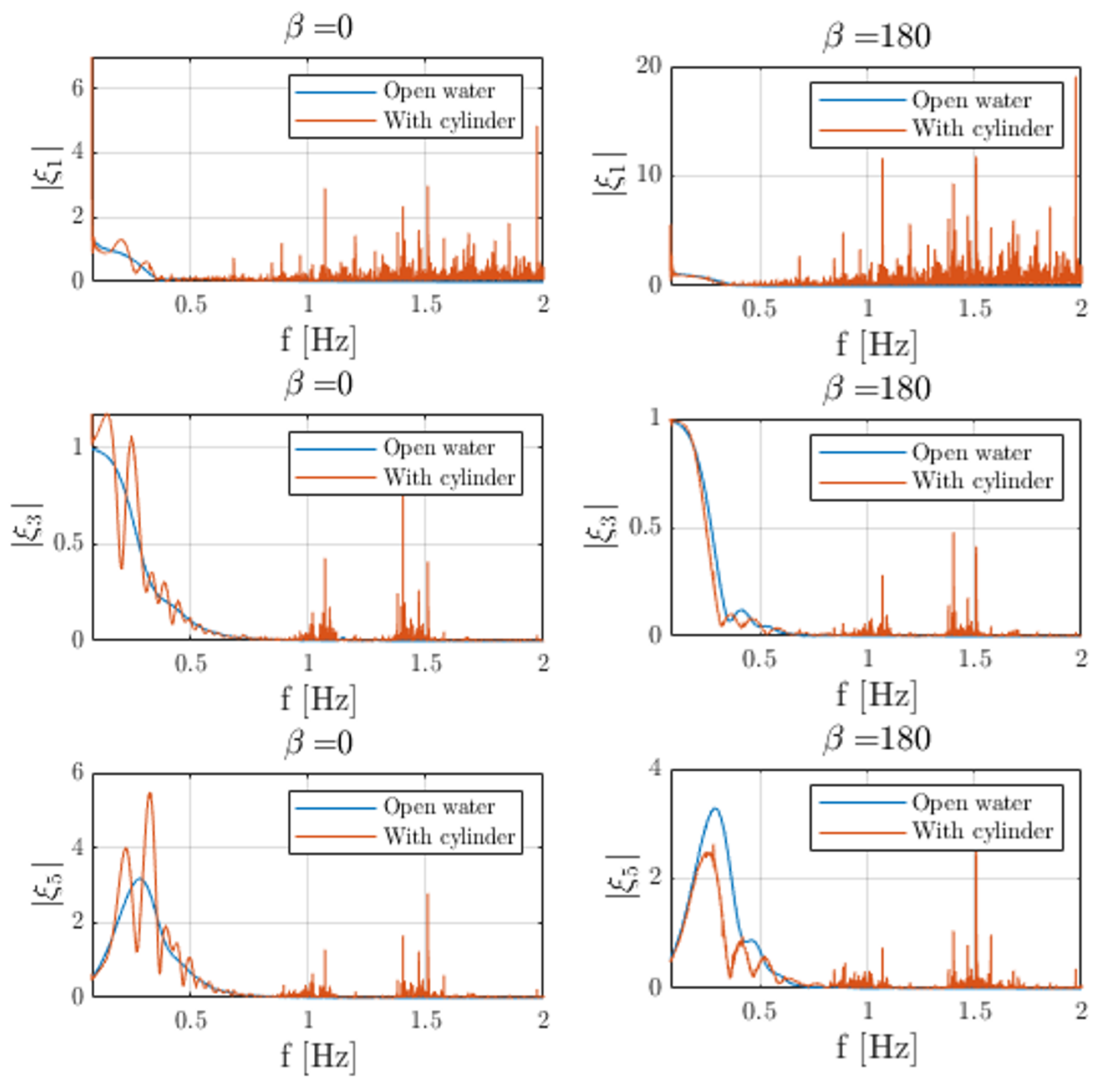
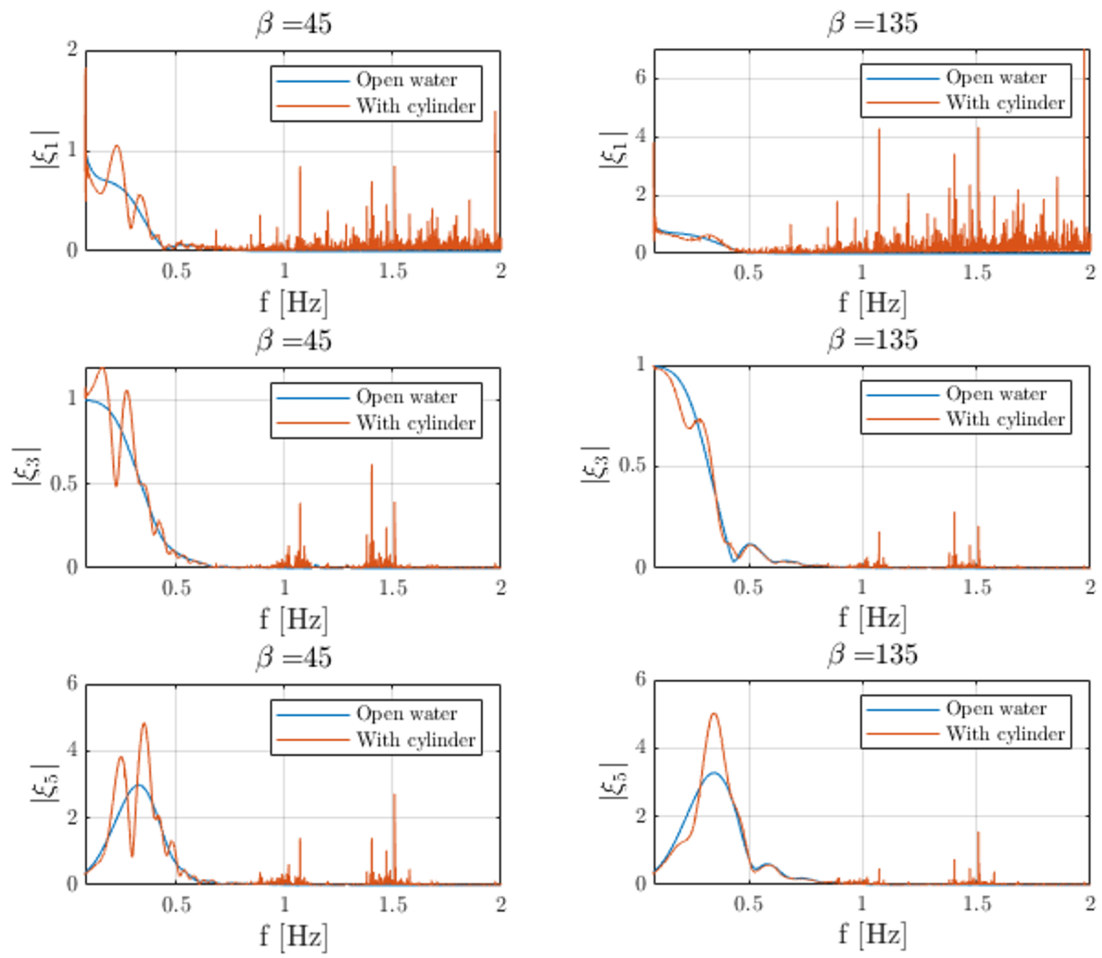Figure 5.13: RAO for ship located 0º and 180º with respect to the incident wave.

Figure 5.14: Longitudinal-vertical plane RAO for β = 45 and β = 135
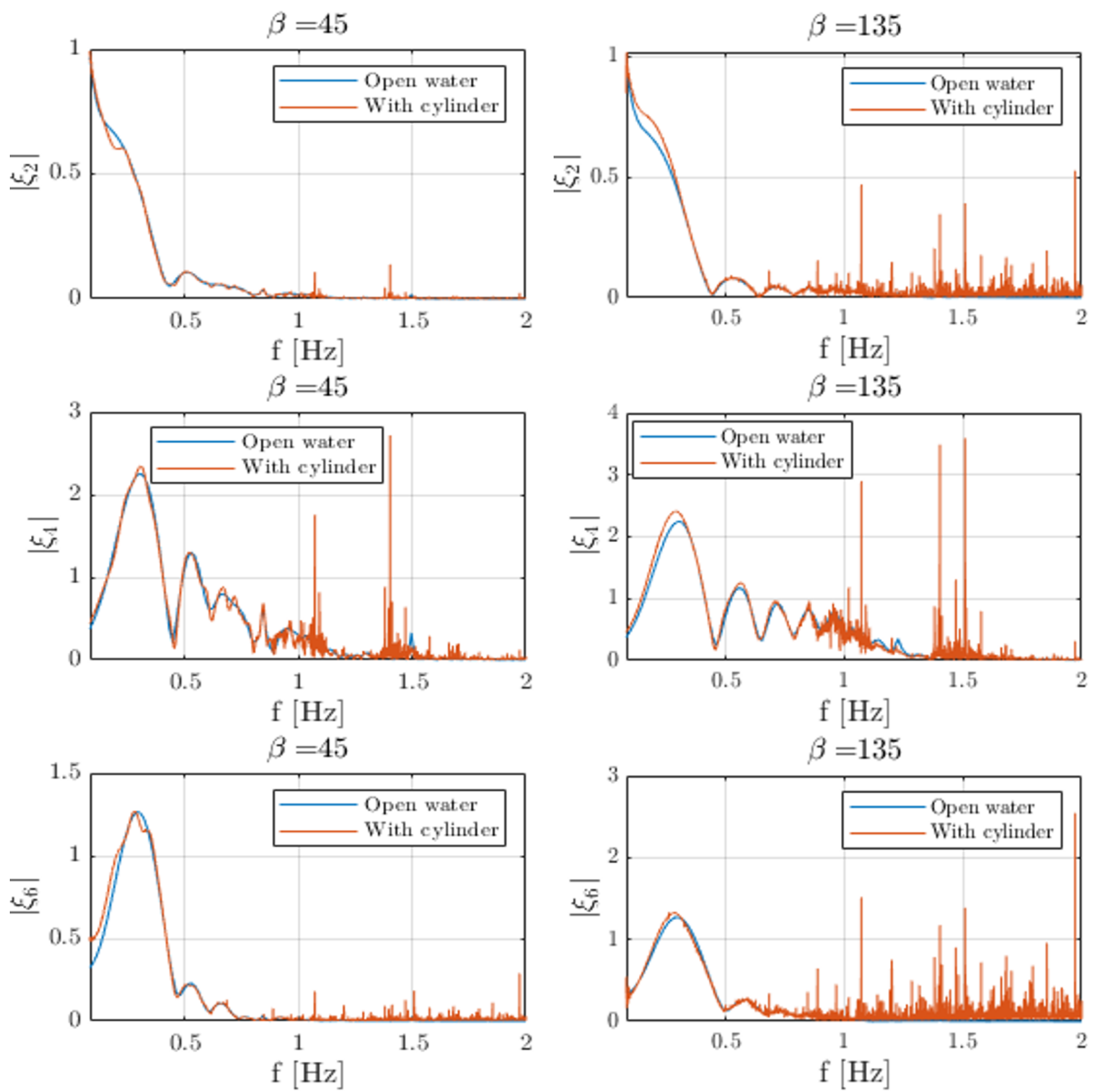
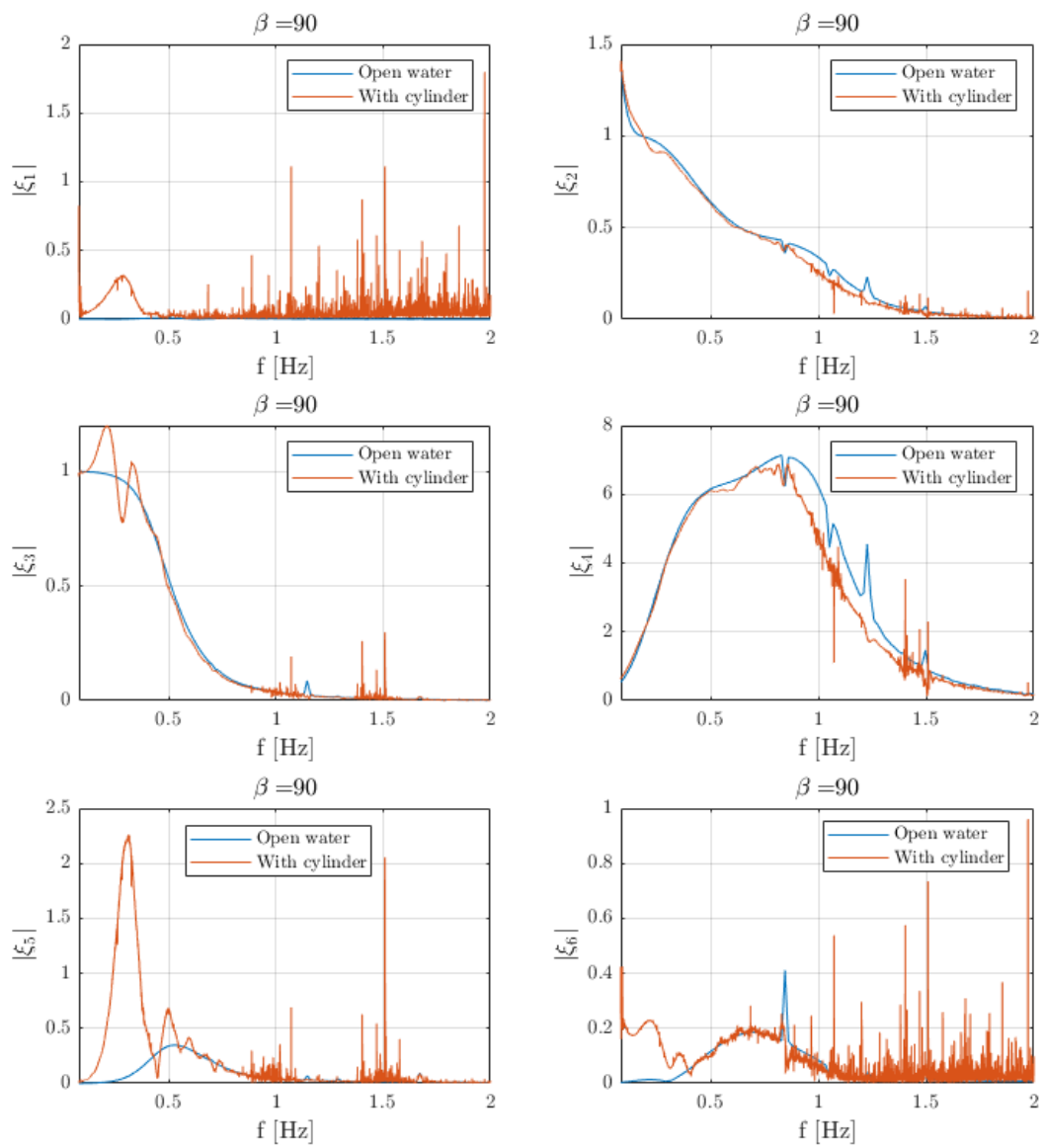Figure 5.15: Transverse-vertical plane RAO for β = 45 and β = 135

Figure 5.16: RAO for ship located 90º with respect to the incident wave.

6 Conclusions and Future Work

In this project, a thorough analysis of ship motions in regular and irregular waves was undertaken, providing insights into the complex dynamics experienced by vessels at sea. The investigation comprised two major sections: one theory based on the diffraction forces set up, validation and application to BEM, and the second part focused on the study of the motions of a traditional Wigley hull and a conceptual workboat hull (including an extension to irregular waves).

The analysis of ship motions in regular waves began by looking into the fundamental principles governing the dynamics of a longitudinally symmetrical ship subjected to waves. By uncoupling the six degrees of freedom and linearizing the equations of motion, the Response Amplitude Operators (RAOs) were derived for different wave frequencies ω and heading angles β. The obtained RAOs provided valuable insights into how the ship responds to wave-induced excitations in both longitudinal and transverse planes.

The subsequent quest extended the analysis to irregular waves, by leaning on linear wave theory and using the JONSWAP spectrum. This allowed diving into the time-domain formulation of the linear wave-structure interaction, incorporating radiation forces, diffraction effects, and their convolution with the incident wave signal. The resulting equations of motion provided a comprehensive understanding of the ship's behaviour in realistic sea conditions.

After examining the flat panel ship's motions under different sea states, observations revealed that the scattered wave field significantly influences specific heading angles: $\beta = 0$ and $\beta = 90$ where the Pitch response stands out among others. However, when placing the ship right behind the wind turbine foundation, i.e. $\beta = 180$, a reduction in the ship's response to essentially every mode of motion takes place. During these particular orientations, the relation between the hull geometry and incoming waves led to amplified ship motions. Recognizing these key heading angles is crucial for the design of vessels ensuring a secure working environment.

There are still some key aspects that require further study. Firstly, there is a need to analyse the scattering contribution of the ship itself. While the project focuses on the impact the scattered waves from the cylinder produce, accounting for the ship's scattering contribution could offer a more complete picture of how waves interact with the vessel. Additionally, the research could be extended by including a non-stationary situation of the ship. However, for the stationary one, the next step would be conducting physical model experiments in FORCETechnology wave tank with the new incorporated code accounting for the scattered wave field.

Lastly, the insights gained from this project have practical implications for the maritime industry, reinforcing the importance of considering scattered wave effects in the pursuit of safer and more efficient marine transportation and operations.

Bibliography

[1]   C. C. Mei. *Theory and applications of ocean surface waves*. Part 1: Linear Aspects. Vol. 23. Advanced Series on Ocean Engineering. World Scientific, 1989.

[2]   Henryk Olszewski and H. Ghaemi. *NEW CONCEPT OF NUMERICAL SHIP MOTION MODELLING FOR TOTAL SHIP OPERABILITY ANALYSIS BY INTEGRATING SHIP AND ENVIRONMENT UNDER ONE OVERALL SYSTEM.* POLISH MARITIMIE RESEARCH, 2018.

[3]   Hans Hersbach et al. "The ERA5 global reanalysis". In: *Quarterly Journal of the Royal Meteorological Society* 146.730 (2020), pp. 1999–2049. ISSN: 0035-9009, 1477-870X. DOI: 10.1002/qj.3803. URL: https://rmets.onlinelibrary.wiley.com/doi/10.1002/qj.3803 (visited on 10/05/2023).

[4]   *IDENTEC SOLUTIONS Wireless Technology. Because It Works*. IDENTEC SOLUTIONS. URL: https://www.identecsolutions.com (visited on 10/03/2023).

[5]   *Wave Heights and Accessibility*. URL: https://windmonitor.iee.fraunhofer.de/windmonitor_en/4_Offshore/3_externe_Bedingungen/3_Wellen/ (visited on 10/03/2023).

[6]   B. Mutlu Sumer and Jørgen Fredsøe. *Hydrodynamics around cylindrical structures*. Revised Edition. Vol. 26. Advanced Series on Ocean Engineering. World Scientific, 2006.

[7]   Harry B. Bingham. *A note on fundamental wave solutions in 2D and 3D*. Oct. 25, 2023.

[8]   Harry B. Bingham and Yanlin Shao. *Wave loads on ships and offshore structures, Lecture notes*. 2023.

[9]   Ulrik Dam Nielsen. *Analysis of ships and other floating structures*. DTU Construct, Technical University of Denmark, 2023.

[10] Harry B. Bingham. *Supplemental Lecture Note for: "Wave Loads on Ships and Offshore Structures"*. Technical University of Denmark, Jan. 16, 2021.

[11] *ProZero DCW 11m Wind farm Service Boat – Prozero*. URL: https://prozero.dk/prozero-dcw-11m/ (visited on 11/17/2023).

Real-Time Simulation of Service Vessels for Offshore Wind Turbine